



# PARITANTRA

Journal of Systems Science  
and Engineering

A PUBLICATION OF  
SYSTEMS SOCIETY OF INDIA

Selected Papers from **NSC-2022:**  
Global Sustainability through  
Lacto-Vegetarian (-cum-Teetotaller)  
Agroecology (-cum-Precision Farming) Systems

**A SPECIAL ISSUE**

# PARITANTRA

Journal of Systems Science and Engineering

Volume 27

Number 1

May 2023

ISSN 0972-5032 (P)



Gram: TECHNOLOGY DELHI  
Telex: 31-73087 IIT IN  
FAX: 91-11-6862037  
Electronic Mail: pss@ee.iitd.ernet.in

**P. S. SATSANGI**

B.Sc. (Elec. Engg. Banaras Hindu University (BHU))  
M.S. (Michigan State University, USA)  
Ph.D. (University of Waterloo, Ontario, Canada)

Professor  
Electrical Engineering Department (EE)  
& Applied Systems Research Programme  
Indian Institute of Technology  
Hauz Khas, New Delhi-110016  
Res. 3, Street C, I.I.T. Estate, New Delhi - 110016  
Phone: Off. 651840, 666979 Ext. 2207, 653561 (EE) Res. 665424

**P. S. SATSANGI**  
Managing Director

**FOUNDATION FOR  
INNOVATION AND  
TECHNOLOGY  
TRANSFER**

Gram: TECHNOLOGY DELHI  
Telex: 31-73087 IIT IN  
Fax: 91-11-6862037  
Phone: Off. 651840, 666979 Ext. 2207  
653561 (EE) Res. 665424

## EDITORIAL BOARD

EMERITUS EDITOR

**Prof. Prem Saran Satsangi**

*Chairman*

Advisory Committee on Education  
Dayalbagh Educational Institutions  
Dayalbagh, Agra 282005

Department of Electrical Engineering, IIT Delhi  
&

*Visiting Post Doctoral Fellow*  
Faculty of Environmental Studies  
University of Waterloo  
(During Summer Quarter 1970  
on Vacation Leave from IIT Delhi)

CHIEF EDITOR

**Prof. Prem Kumar Kalra**

*Professor & Head*

Department of Computer Science and Engineering, IIT Delhi  
*President, Systems Society of India*

## EDITORIAL ADVISORY BOARD

- **Prof. Anand Srivastava**  
Professor  
Department of Mathematics  
University of Kiel
- **Prof. Prem Kumar Kalra**  
Director/Vice-Chancellor  
Dayalbagh Educational Institute
- **Prof. Anna Margaretha Horatschek**  
Professor Emeritus  
Department of English  
University of Kiel
- **Prof. Peter Roe**  
Professor Emeritus  
Department of Systems Design Engineering  
University of Waterloo
- **Prof. Karmeshu**  
Distinguished Professor  
University of Petroleum and Energy Studies  
Honorary Professor, Shiv Nadar University
- **Prof. Siddhartha Mukhopadhyay**  
Professor  
Department of Electrical Engineering  
IIT Kharagpur

- **Prof. Gordon Savage**  
Professor  
Department of Systems Design Engineering  
University of Waterloo
- **Prof. D. Anand Rao**  
Retired Professor  
Department of Electrical Engineering  
Dayalbagh Educational Institute
- **Prof. Pami Dua**  
Director/Vice-Chancellor  
Delhi School of Economics  
University of Delhi
- **Dr. Bani Dayal Dhir**  
Assistant Professor  
Department of English Studies  
Dayalbagh Educational Institute
- **Prof. C. Patvardhan**  
Professor  
Department of Electrical Engineering  
Dayalbagh Educational Institute
- **Prof. Huzur Saran**  
Professor  
Department of Computer Science and Engineering  
IIT Delhi
- **Prof. Vishal Sahni**  
Retired Professor  
Department of Electrical Engineering  
Dayalbagh Educational Institute
- **Dr. Dayal Pyari Srivastava**  
Assistant Professor  
Department of Physics and Computer Science  
Dayalbagh Educational Institute
- **Dr. Prem Sewak Sudhish**  
Associate Professor  
Department of Physics and Computer Science  
Dayalbagh Educational Institute
- **Prof. V.B. Gupta**  
Editor, ODL Newsletter  
Vice Chairman, Advisory Committee on Education  
Coordinator, Distance Education Program,  
Dayalbagh Educational Institute

### EDITORIAL COORDINATOR

**Prof. D. Bhagwan Das**  
Professor, Department of Electrical Engineering  
Dayalbagh Educational Institute (Deemed to be University)  
Dayalbagh, Agra 282005, INDIA  
(email: systems.society@gmail.com)

### Published by

**Systems Society of India**  
IT Centre, DEI ICT Distance Education Centre  
Dayalbagh Educational Institute (Deemed to be University)  
Model School, Soami Nagar, New Delhi 110017

*Copyright © 2023, Systems Society of India. All rights reserved. No part of this publication may be reproduced, stored, transmitted, or disseminated in any form, or by any means, without prior written permission from the Editorial Office, to whom all requests to reproduce copyright material should be directed.*

# PARITANTRA

Journal of Systems Science and Engineering

## Aims and Scope

This journal publishes original research and advancement in the field of theory and applications of systems science and engineering. The journal is primarily devoted to unification of themes, cross fertilization of ideas, identification and characterization of underlying quantitative and qualitative features of problem formulation and general solution; and solution of multi-level interdisciplinary socio-economic, engineering-economic and real-world problems in the context of national/global development. The journal has a very wide scope which includes applied systems research, systems modelling methodology, socio-economic and environmental systems, operational research and management, informatics, artificial intelligence and soft systems including literary systems and theology ("Better Worldliness").

## Manuscript Preparation

Authors are requested to prepare their manuscripts using a standard manuscript format template provided on the SSI website: [www.sysi.org](http://www.sysi.org) in MS word.

## Submission

Papers may be submitted electronically to the Editorial Coordinator.  
(email: [systems.society@gmail.com](mailto:systems.society@gmail.com))

PARITANTRA Journal of Systems Science and Engineering has a priority access to papers presented at meetings organized or sponsored by SSI. These papers may need an extension and further review before they are ready for publication. In addition, the journal may bring a special issue with papers which obtain the best paper awards during the presentations in a (Inter) National Systems Conference. The journal also encourages special issues on emerging themes in systems science and engineering, a proposal for which should be submitted to the Chief Editor through the Editorial Coordinator.

## Copyright

All authors must sign the Transfer of Copyright Agreement before the article can be published. This transfer agreement enables SSI to protect the copyrighted material for the authors, without affecting the authors' proprietary rights. The copyright transfer covers the exclusive rights to reproduce and distribute the article, including reprints, photographic reproductions, microfilm or any other reproductions of similar nature and translations, and includes the right to adapt the article for use in conjunction with computer systems and programs, including reproduction or publication in machine-readable form and incorporation in retrieval systems. Authors are responsible for obtaining from the copyright holder permission to reproduce any figures or other material included in the paper for which copyright already exists.

# Editorial

## Selected Papers from NSC-2022: Global Sustainability through Lacto-Vegetarian (-cum-Teetotaller) Agroecology (-cum-Precision Farming) Systems

### A SPECIAL ISSUE

The forty-fifth (Inter) National Systems Conference (NSC 2022) was co-organized with the fourth International Dayalbagh Science of Consciousness Conference (DSC 2022) on 26<sup>th</sup> – 29<sup>th</sup> September 2022 at Dayalbagh Educational Institute in partnership with the Systems Society of India. The conference was organized in hybrid mode on the theme “Global Sustainability through Lacto-Vegetarian (-cum-Teetotaller) Agroecology (-cum-Precision Farming) Systems”.

DEI, SSI and the NSC-2022 Program and Organising Committee most humbly submit their deep gratitude for the inspiration, blessings, guidance and direction received from Revered Prof. P.S. Satsangi Sahab, Founding President of the Systems Society of India; Chairman of the Advisory Committee on Education for Dayalbagh Educational Institutions (a non-statutory body constituted to serve as a think-tank to suggest inter-alia steps necessary for achieving highest levels of excellence); and the Chief Patron for the 45<sup>th</sup> (Inter) National Systems Conference, 2022.

A call for papers for the conference was published several months in advance on the websites of Dayalbagh Educational Institute and the Systems Society of India that attracted submission of 129 research papers. All submissions were reviewed by multiple reviewers drawn from a pool of experts in respective areas, based on which thirty-six submissions were selected for oral presentations, divided into six sessions in different broad areas with six papers each, while another forty-one submissions were shortlisted for poster presentations. The authors had the option to present their paper in-person or through a pre-recorded video of 8 minutes duration for oral presentation and 3 minutes duration for poster presentation, followed by live audio interaction with questions and answers. Finally, thirty-six oral papers and thirty-two posters were presented. The session chairs adjudged the best paper presented in their respective session.

The conference had three plenary talks by internationally reputed systems scientists in different areas — Prof. Ray Ison, President, International Federation for Systems Research; Dr. S Unnikrishnan Nair, Director, Vikram Sarabhai Space Centre; and Prof. Ashwani Pareek, Executive Director, National Agri-Food Biotechnology Institute. The awards for best papers and the annual awards of the Systems Society of India were presented at the joint awards ceremony for the two conferences. The joint conference concluded with a lively panel discussion, where each panelist presented views on the questions set forth by the moderator, based on their individual expertise. This was followed by a short cultural programme presented by the students of the Dayalbagh Educational Institute.

This Special Issue is prepared with six papers that received the best paper award in each of the six oral sessions corresponding to the six categories – Agroecology Systems; Consciousness based and Literary Systems; Energy Systems; Environment Systems; Healthcare Systems; and Information and Communication Systems. The papers were duly revised for publication in this issue.

We sincerely appreciate the efforts of all authors in contributing to this Special Issue. We would also like to express our deep gratitude to the Editorial Board of the journal PARITANTRA for supporting and sponsoring this Special Issue. We also gratefully acknowledge competent assistance from Dr. Priti Gupta, IIT Delhi for copy editing and proofreading and Mrs. Aruna Sharma for design and layout.

**- NSC-2022 Program and Organising Committee**

# PARITANTRA

Journal of Systems Science and Engineering

Volume 27

Number 1

May 2023

ISSN 0972-5032 (P)

## Selected Papers from NSC 2022 on Global Sustainability through Lacto-Vegetarian (-cum-Teetotaler) Agroecology (-cum-Precision Farming) Systems

A SPECIAL ISSUE

### Contents

Simulation of Water and Nutrient Distribution in Raised Bed Onion under Different Soil Types, Emitter Discharge Rates and Irrigation Intervals <b>P.R. Anjitha Krishna, B. Maheshwara Babu, A.T. Dandekar, R.H. Rajkumar, G. Ramesh and S.R. Balanagoudar</b>	1
Empirical Measurement of Aesthetic Experience of Music <b>Abhishek Gupta and C.M. Markan</b>	7
Role of Thermal Annealing in Fabrication of Bismuth Ferrite Thin Films for Photoelectrochemical Water Splitting <b>Bhanupriya, Kumari Ruchi, Runjhun Dutta, Anuradha Verma, Anupam Srivastav, Manju Srivastava and Rohit Shrivastav</b>	11
Comparative Analysis of Fine Particulate Matter (PM <sub>2.5</sub> ) over the Indo Gangetic Plain (IGP) in the Era of COVID-19: Normal to the New Normal <b>Isha Goyal, Muskan Agarwal, Simran Bamola, K. Maharaj Kumari and Anita Lakhani</b>	16
Prosthetics Advice, Design and Fabrication using Digital Manufacturing Systems for Improved Healthcare Systems <b>Guru Ratan Satsangee, Bobby Tyagi, Dheeraj Kumar Angajala, Ankit Sahai and Rahul Swarup Sharma</b>	22
Femtosecond Photonic Logic Gates with MoTe <sub>2</sub> Nanocomposite Thin Films <b>Anam Saifi and Sukhdev Roy</b>	29
<b>Appendix: NSC-2022 Conference Committee</b>	<b>34</b>

# Simulation of Water and Nutrient Distribution in Raised Bed Onion under Different Soil Types, Emitter Discharge Rates and Irrigation Intervals

P. R. Anjitha Krishna<sup>1\*</sup>, B. Maheshwara Babu<sup>2</sup>, A. T. Dandekar<sup>2</sup>, R. H. Rajkumar<sup>2</sup>, G. Ramesh<sup>3</sup> and S. R. Balanagoudar<sup>2</sup>

<sup>1</sup>Department of Agricultural Engineering,  
Dayalbagh Educational Institute, Agra, 282005, Uttar Pradesh, India

<sup>2</sup>Department of Soil and Water Conservation Engineering,

<sup>3</sup>Department of Horticulture,  
University of Agricultural Sciences, Raichur, 584104, Karnataka, India

*Simulation of water and solute (ammonium, nitrate) movement in the root zone of raised bed onion with drip fertigation and mulching was done with calibrated and validated HYDRUS-2D model by considering different soil types (clay, clay loam, loam, sandy loam and silt loam), emitter discharge rates (2&4 litres per hour (lph)) and irrigation intervals (2, 4 and 7 days). Drip fertigation with 2 lph emitter and two days of irrigation interval was found to be the most appropriate management option with different soil types to reduce leaching of water and solutes and to obtain maximum root uptake of water and nutrients. The time required to leach 1000 cm<sup>3</sup> of water under this scenario for different soil types were found to be 64.65, 36.44, 13.16, 8.26 and 2.72 days after the first irrigation for clay, clay loam, loam, silty loam and sandy loam soil types, respectively. Leaching of nitrate started at 19.74, 15.39, 10.33, 9.36, 7.94 days after the first fertigation from clay, clay loam, loam, silty loam and sandy loam soils, respectively. The percent of leaching of water and nitrate by the end of the season from clay, clay loam, loam, silty loam and sandy loam soils was 7.31 & 0.6%, 14.36 & 1.47%, 22.57 & 2.88%, 25.3 & 3.42% and 29.99 & 4.64%, respectively. HYDRUS-2D was found to be an efficient management tool for scenario generation for crop cultivation in semi-arid conditions after proper calibration and validation.*

**Keywords** - HYDRUS, Mulch, Onion, Semi-arid, Solute transport

## I. INTRODUCTION

Considering the dynamic behaviour of hydraulic properties of water and soil, drip design scenarios can be improved, which demands extensive and elaborative research and resource requirements. Numerical modeling techniques serve as a solution in this aspect. Drip fertigation synchronizes the irrigation and plant nutrients application which meets the crop requirements by maintaining proper water and nutrient concentration in the crop root zone [22]. The synchrony between nutrient supply and crop requirement is essential to ensure adequate quantity of uptake, its utilization and optimum yield [11]. The increasing trend of environmental pollution from agricultural and non-agricultural sectors points towards need of improved management practices for letting the contaminants away from groundwater and surface water sources. Once released into the environment, point or non-point sources of contaminants are subjected to simultaneous physical, chemical, and biological processes, including advective-dispersive transport, sorption-desorption, volatilization, precipitation-dissolution, complexation and

biodegradation. The numerical models allow consideration of large number of simultaneous non-linear processes to simulate the real scenarios, and to study the effect of various geophysical conditions on these processes.

The distribution of water and solutes under drip irrigation system differs from surface irrigation system, as the movement happens around the emitter with comparatively smaller wetted volume with frequent application of irrigation. It makes, one dimensional simulations inadequate to represent the transient infiltration process occurring in a three dimensional space [8]. The soil moisture regime around the point source and the dynamics of associated solutes depends on parameters like emitter discharge rate, soil hydraulic properties, plant root distribution and plant uptake patterns [9], [21]. Modeling of solute transport in the vadoze zone (the entire zone of negative water pressure above the water table (permanent or seasonal)), enrich the understanding of their movement in soils and nutrient uptake by plants and it serves as a valuable tool in the design of drip fertigation system [19]. In the present study, it is envisaged to collect the data pertaining to water and nutrient distributions under mulched and non-mulched drip fertigation system with a highly potential horticulture crop in India, i.e. onion.

\*Corresponding author: [anjithakrishna@dei.ac.in](mailto:anjithakrishna@dei.ac.in)  
ISSN 0972-5032; Copyright ©2023, SSI

## II. MATERIALS AND METHODS

In the present study, the soil water movement and transport of available soil N were simulated in calibrated HYDRUS-2D model under various scenarios comprising of different soil types (clay, clay loam, loam, sandy loam and silty loam), two emitter discharge rates (2 and 4 lph with emitter spacing of 20 cm) and three irrigation intervals (2, 4 and 7 days) for raised bed onion cultivation in plastic mulched condition with thirteen weekly doses of fertigations at fully recommended dose of fertilizers (125:50:125:50 kg ha<sup>-1</sup> of N:P:K:S). The conceptual diagram of simulation domain for the water movement simulation with the imposed boundary conditions is shown in Fig. 1. The soil hydraulic properties for different soil types were chosen from Rosetta Lite v.1.1 inbuilt in HYDRUS. The variable flux boundary for the 2 and 4 lph emitter discharges were taken as 12 and 17 cm, respectively based on field trials.

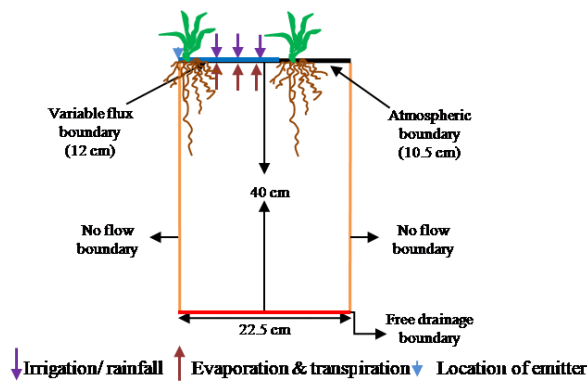


Fig. 1. Conceptual representation of modeling domain with boundary condition

## III. RESULTS AND DISCUSSION

### A. Water movement

The percent of root uptake and percent of leaching are derived out of the total applied and initial water present in the domain. In case of emitter discharge rate of 2 lph, the percent leaching of water increased with increasing irrigation interval. In all the irrigation intervals, leaching of water was highest from the sandy loam soil (29.99, 30.78 and 34.35% for 2, 4 and 7 days irrigation intervals, respectively) due to low water holding capacity of the soil and higher hydraulic conductivity. The leaching was least from clay soil in all the irrigation intervals due to higher soil moisture retention by capillary forces (Table I-III)

The discharge rate of 4 lph from emitters placed at 20 cm spacing resulted in tremendous wastage of irrigated water in all the treatments under different irrigation intervals. Increased wetted volume under 4 lph emitter compared to 2 lph emitter is reported by [1] and [5]. The leaching percentage decreased with increasing irrigation interval as high application rate per irrigation results in high

leaching. The lowest leaching and highest root water uptake was observed under two days irrigation interval with 2 lph emitter discharges in clay soil. Significant influence of irrigation frequency in soil water distribution was reported by [18]. High leaching fraction from sandy loam soil and increased leaching with increased emitter discharge rates is already reported [2]. The effect of gravity force greatly governs the moisture movement in coarse textured soil, which might have resulted in greater percolation. The capillary forces dominant in fine textured soils might help in more lateral spread of moisture and reduced percolation [24]

TABLE I  
EFFECT OF SOIL TYPES ON WATER UPTAKE AND LEACHING AT 2 DAYS IRRIGATION INTERVAL

Soil type	% root uptake		% leaching	
	2 lph	4 lph	2 lph	4 lph
Clay	48.52	21.50	7.31	56.13
Clay loam	48.51	27.27	14.36	50.85
Loam	48.51	21.50	22.57	63.50
Sandy loam	48.51	21.50	29.99	67.31
Silty loam	48.53	21.50	25.30	64.46

TABLE II  
EFFECT OF SOIL TYPES ON WATER UPTAKE AND LEACHING AT 4 DAYS IRRIGATION INTERVAL

Soil type	% root uptake		% leaching	
	2 lph	4lph	2 lph	4lph
Clay	47.98	21.17	8.24	54.14
Clay loam	47.98	26.86	15.35	48.14
Loam	47.97	21.17	23.46	62.81
Sandy loam	47.98	21.17	30.78	68.03
Silty loam	47.99	21.18	26.22	65.24

TABLE III  
EFFECT OF SOIL TYPES ON WATER UPTAKE AND LEACHING AT WEEKLY IRRIGATION INTERVAL

Soil type	% root uptake		% leaching	
	2 lph	4lph	2 lph	4lph
Clay	44.73	19.22	13.19	51.96
Clay loam	44.73	24.38	19.69	45.62
Loam	44.72	19.25	27.26	60.89
Sandy loam	44.73	19.25	34.35	70.92
Silty loam	44.74	19.25	29.70	68.21

**B. Solute transport**

**a. Available soil nitrogen**

The 2 lph emitters at 20 cm spacing resulted in highest leaching percentage of 9.6% in weekly irrigations from sandy loam soil. Reference [14] reported leaching of 4.3% from sandy loam under alternate day irrigation, which is in agreement with the result. The root water uptake percentage from different soil types was in the range of 54 to 69%. The leaching of nitrate from clay soil at two and four days irrigation interval was negligible (0.6 and 0.78%). Among the soil types highest root solute uptake was observed in sandy loam soil, but with a high leaching percentage with 2 lph emitter discharge (Table IV-VI), which is in conformity with previously published findings [10], [16]. The reported onion growth and yield characteristics from sandy loam soil were better than in clay or clay loam soils [6], [7], [22], [23].

From Table IV-VI, it can be observed that the higher emitter discharge rates at a closer emitter spacing may result in loss of 40 to 62% of the applied nitrogen by leaching of nitrate below the crop root zone. Reference [2] reported higher nitrogen leaching under sandy loam soil with 4 lph emitter discharge compared to clay and silty soils. About 32.3 to 40.9% of nitrogen loss under mulched conditions was reported under 4 lph emitter discharge from sandy loam soil type [15]. The soil types, emitter discharge rates and irrigation interval had significant effect on cumulative leaching of nitrogen below 40 cm soil depth. The simulation considered hydrolysis, nitrification and adsorption of ammonia, but neglected denitrification process.

Ammonium concentration was restricted close to top soil layers near to emitter, and the concentrations reached to insignificant levels within two days of fertigation. Strong absorption of ammonium by the soil and rapid nitrification process might have restricted the ammonium concentration to the vicinity of emitter, as suggested by [13]. The nearness of the concentrations to the bottom of the simulation domain indicates leaching and loss of the solutes (Fig. 2-5). Ammonium and phosphorus retained within the crop root zone throughout the simulation period. Nitrate and potassium were prone to leaching especially under the 4 lph emitter with seven days of irrigation interval (Fig. 5). Continuous downward movement of nitrate was observed during the whole simulation period due to presence of higher amount of water inputs and lack of absorption from soil solids. Similar distribution pattern of nitrogen was reported in previous experiments [2], [3], [12].

**TABLE IV**  
EFFECT OF SOIL TYPES ON NITRATE UPTAKE AND LEACHING AT 2 DAYS IRRIGATION INTERVAL

Soil type	% root uptake		% leaching	
	2 lph	4lph	2 lph	4lph
Clay	60.05	25.25	0.60	46.70

Clay loam	62.43	30.00	1.47	42.79
Loam	65.25	26.35	2.88	54.35
Sandy loam	69.19	27.48	4.64	57.83
Silty loam	66.18	26.54	3.42	55.30

**TABLE V**  
EFFECT OF SOIL TYPES ON NITRATE UPTAKE AND LEACHING AT 4 DAYS IRRIGATION INTERVAL

Soil type	% root uptake		% leaching	
	2 lph	4lph	2 lph	4lph
Clay	59.03	26.27	0.78	44.24
Clay loam	61.67	31.05	1.70	39.68
Loam	64.47	27.40	3.21	52.85
Sandy loam	68.55	28.62	4.97	57.20
Silty loam	65.43	27.25	3.83	55.04

**TABLE VI**  
EFFECT OF SOIL TYPES ON NITRATE UPTAKE AND LEACHING AT WEEKLY IRRIGATION INTERVAL

Soil type	% root uptake		% leaching	
	2 lph	4lph	2 lph	4lph
Clay	54.42	24.40	2.53	45.27
Clay loam	56.61	28.96	4.13	39.74
Loam	59.04	25.58	6.59	54.35
Sandy loam	62.50	26.02	9.61	61.44
Silty loam	59.90	24.47	7.46	59.77

**b. Movement of soil water and solutes under different simulation scenarios**

The major advantage associated with the drip irrigation system is its ability to manage leaching of soil water and soil solutes to a minimum concentration. A calibrated and validated HYDRUS-2D model can be used to gather information on complex soil processes to make better management policies. The movement of soil water and solutes (ammonium and nitrate) under different simulation scenarios are presented in Table VII-XI.

**TABLE VII**  
RESULTS OF WATER AND NITRATE MOVEMENT IN CLAY SOIL

Simulation scenario	Time to cross leaching of 1000 cm <sup>3</sup> water (days*)	Time to start leaching of nitrate (days**)
Clay-2 lph-2 days	64.65	19.74
Clay-2 lph-4 days	58.55	17.14
Clay-2 lph-7 days	48.52	14.72

Clay-4 lph-2 days	16.67	6.79
Clay-4 lph-4 days	14.15	3.86
Clay-4 lph-7 days	13.77	2.68

[day\*: days after 1<sup>st</sup> irrigation; day\*\*: days after 1<sup>st</sup> fertigation]

**TABLE VIII**  
RESULTS OF WATER AND NITRATE MOVEMENT IN CLAY LOAM SOIL

Simulation scenario	Time to cross leaching of 1000 cm <sup>3</sup> water (days*)	Time to start leaching of nitrate (days**)
Clay loam-2 lph-2 days	36.44	15.39
Clay loam-2 lph-4 days	34.18	12.82
Clay loam-2 lph-7 days	29.83	10.86
Clay loam-4 lph-2 days	16.56	7.38
Clay loam-4 lph-4 days	13.99	4.06
Clay loam-4 lph-7 days	12.50	2.99

**TABLE IX**  
RESULTS OF WATER AND NITRATE MOVEMENT IN LOAM SOIL

Simulation scenario	Time to cross leaching of 1000 cm <sup>3</sup> water (days*)	Time to start leaching of nitrate (days**)
Loam-2 lph-2 days	13.16	10.33
Loam-2 lph-4 days	11.41	8.29
Loam-2 lph-7 days	9.89	5.38
Loam-4 lph-2 days	6.79	3.26
Loam-4 lph-4 days	5.61	2.48
Loam-4 lph-7 days	3.45	2.23

**TABLE X**  
RESULTS OF WATER AND NITRATE MOVEMENT IN SILTY LOAM SOIL

Simulation scenario	Time to cross leaching of 1000 cm <sup>3</sup> water (days*)	Time to start leaching of nitrate (days**)
Silty loam-2 lph-2 days	8.26	9.36
Silty loam-2 lph-4 days	7.36	7.56
Silty loam-2 lph-7 days	6.17	4.65
Silty loam-4 lph-2 days	4.98	2.91
Silty loam-4 lph-4 days	4.33	2.39
Silty loam-4 lph-7 days	2.18	2.20

**TABLE XI**  
RESULTS OF WATER AND NITRATE MOVEMENT IN SANDY LOAM SOIL

Simulation scenario	Time to cross leaching of 1000 cm <sup>3</sup> water (days*)	Time to start leaching of nitrate (days**)
Sandy loam-2 lph-2 days	2.72	7.94
Sandy loam-2 lph-4 days	2.34	5.31
Sandy loam-2 lph-7 days	1.40	3.64
Sandy loam-4 lph-2 days	1.99	1.64
Sandy loam-4 lph-4 days	1.23	1.44
Sandy loam-4 lph-7 days	0.52	1.95

Minimum leaching of soil water and solutes were observed with the clay soil with 2 lph emitter and two days of irrigation. It can be inferred that it may take 64.65 days after the first irrigation to leach 1000 cm<sup>3</sup> of water below the simulation domain (Table VII). Higher irrigation interval resulted in early leaching of soil water and solutes in all the soil types. The maximum leaching of water and solutes were recorded with the sandy loam soil with 4 lph emitter and seven days of irrigation interval. For the leaching of 1000 cm<sup>3</sup> of water 12.48 hours was sufficient under this scenario.

Also, the leaching of nitrate started after 1.95 days after first fertigation event. Similar lines of information were not obtained in earlier studies with onion. Variation in model predictions from field observations can be expected due to assumptions of time independency of soil hydraulic parameters, uncertainty in solute transport parameters, structural variations in soil profile, ignoring of macro pore effect and bioturbation processes within the soil [12] [25]-[26].

**C. Operation and management guidelines for onion cultivation in different soil types**

From the results of model simulation, it can be confirmed that an emitter of 2 lph discharge rate and two days of irrigation interval may result in minimum loss of water and nutrients with good root uptakes and soil distribution. In the simulations the emitters were placed at 20 cm spacing (equivalent to 4 lph emitter at 40 cm spacing) on the laterals and two laterals were placed on raised beds at a spacing of 45 cm. Fertigations were done on thirteen equal weekly split doses with 15 minutes of irrigation followed by fertigation then 5 minutes of irrigation for flushing of the pipelines. Immediate flushing of drip lines after fertigation was recommended by [17] to reduce nutrient leaching. An emitter discharge of < 4 lph was suggested by [20] in heavy soil.

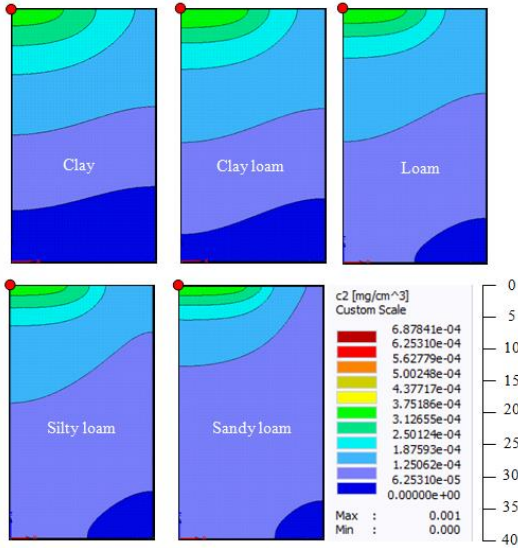


Fig. 2 Distribution of nitrate in the crop root zone in different soil types under 2 lph emitter discharge with 2 days irrigation interval at the end of simulation period.

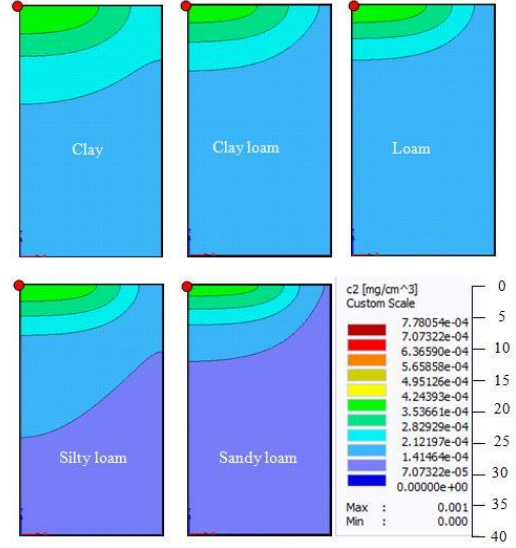


Fig. 4. Distribution of nitrate in the crop root zone in different soil types under 4 lph emitter discharge with 2 days irrigation interval at the end of simulation period.

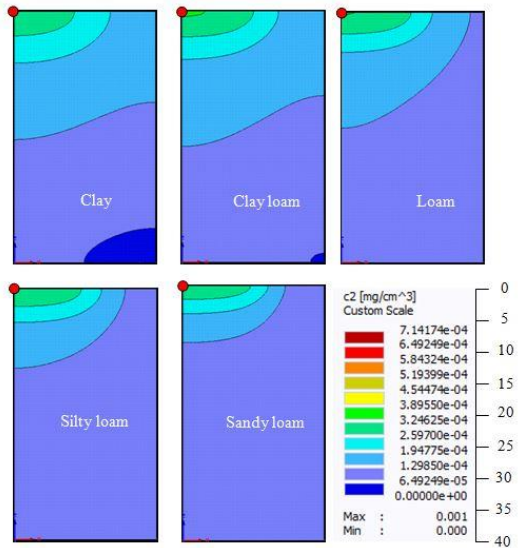


Fig. 3. Distribution of nitrate in the crop root zone in different soil types under 2 lph emitter discharge with 7 days irrigation interval at the end of simulation period.

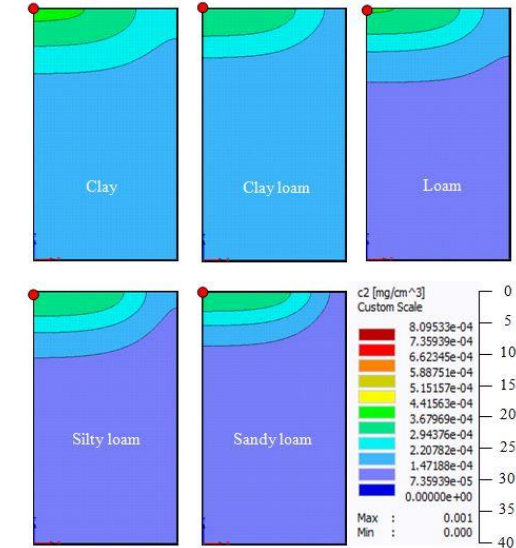


Fig. 5. Distribution of nitrate in the crop root zone in different soil types under 4 lph emitter discharge with 7 days irrigation interval at the end of simulation period.

#### IV. CONCLUSION

HYDRUS-2D model was used for generating simulation scenarios on raised bed onion cultivation in plastic mulch with drip fertigation. An emitter of 2 lph discharge rate and two days of irrigation interval may result in minimum loss of water and nutrients with good root uptakes and soil distribution of soil water and nutrients in the root zone of raised bed onion under mulching and drip fertigation in

clay, clay loam, loam, sandy loam and silty loam soil types. In the simulations the emitters were placed at 20 cm spacing (equivalent to 4 lph emitter at 40 cm spacing) on the laterals and two laterals were placed on raised beds at a spacing of 45 cm. Fertigations were done on thirteen equal weekly split doses with 15 minutes of irrigation followed by fertigation then 5 minutes of irrigation for flushing of the pipelines.

## ACKNOWLEDGEMENTS

The authors are highly grateful to All India Coordinated Research Project (AICRP) on Plasticulture Engineering and Technology for the financial assistance in carrying out the experiment during 2018-2020. Also, the first author thanks the Indian Council of Agricultural Research (ICAR) for providing the Senior Research Fellowship (SRF) fellowship during her doctoral study.

## REFERENCES

- [1] Acar, B., Topak, R., & Mikailsoy, F. (2009). Effect of applied water and discharge rate on wetted soil volume in loam or clay-loam soil from an irrigated trickle source. *African J of Agrl Res.*, 4(1), 49-54.
- [2] Ajdary, K., Singh, D. K., Singh, A. K., & Khanna, M. (2007). Modeling of nitrogen leaching from experimental onion field under drip fertigation. *Agrl. Water Manag.*, 89(1&2), 15-28. <https://doi.org/10.1016/j.agwat.2006.12.014>
- [3] Amin, M. M., Šimůnek, J., & Laegdsmand, M. (2014). Simulation of the redistribution and fate of contaminants from soil-injected animal slurry. *Agrl. Water Manag.*, 131(1), 17-29. <https://doi.org/10.1016/j.agwat.2013.09.002>
- [4] Assouline, S. (2002). The effect of microdrip and conventional drip irrigation on water distribution and uptake. *Soil Sci. Soc. Am. J.*, 66(1), 1630-1636. <https://doi.org/10.2136/sssaj2002.1630>
- [5] Badni, N., Hamoudi, S., Alazba, A. A., & Elnesr, M. N. (2018). Simulations of soil moisture distribution patterns between two simultaneously working surface drippers using Hydrus-2D/3D model. *Int. J. of Engg. and Tech.*, 10(2), 586-595. <http://dx.doi.org/10.21817/ijet/2018/v10i2/181002076>
- [6] Bairagi, P., Yadav, S. R., & Kumar, D. (2015). Response of onion (*Allium cepa* L.) to different levels of NPK and FYM under arid condition of Rajasthan. *An Asian J. of Soil Sci.*, 10(1), 42-46. <https://doi.org/10.15740/HAS/AJSS/10.1/42-46>
- [7] Basha, D. R., Lakshmi, L. M., Sadarunnisa, S., & Venkataramana, K. T. (2018). Genetic variability studies for yield and yield components in Onion (*Allium cepa* L.) genotypes. *Int. J. of Pure and App. Biosci.*, 6(5), 1140-1146. <http://dx.doi.org/10.18782/2320-7051.7072>
- [8] Bresler, E. (1975). Two-dimensional transport of solutes during non-steady infiltration from a trickle source. *Soil Sci. Soc. of Amer. J.*, 39(4), 604-613. <https://doi.org/10.2136/sssaj1975.03615995003900040014X>
- [9] Coelho, E. F., & Or, D. (1999). Root distribution and water uptake patterns of corn under surface and subsurface drip irrigation. *Plant Soil*, 206(1), 123-136. <https://doi.org/10.1023/A:1004325219804>
- [10] Elsbah, R., Selim, T., Mirdan, A., & Berndtsson, R. (2019). Modeling of fertilizer transport for various fertigation scenarios under drip irrigation. *Water*, 11(5), 1-15. <https://doi.org/10.3390/w11050893>
- [11] Fageria, N. K., & Baligar, V. C. (2005). Enhancing nitrogen use efficiency in crop plants. *Adv. in Agron.*, 88(1), 97. [https://doi.org/10.1016/S0065-2113\(05\)88004-6](https://doi.org/10.1016/S0065-2113(05)88004-6)
- [12] Filipović, V. et al. (2016). Plastic mulch and nitrogen fertigation in growing vegetables modify soil temperature, water and nitrate dynamics: experimental results and a modeling study. *Agrl. Water Manag.*, 176(1), 100-110. <https://doi.org/10.1016/j.agwat.2016.04.020>
- [13] Hanson, B. R., Šimůnek, J., & Hopmans, J. W. (2006). Evaluation of urea-ammonium-nitrate fertigation with drip irrigation using numerical modeling. *Agrl. Water Manag.*, 86(2), 102-113. <https://doi.org/10.1016/j.agwat.2006.06.013>
- [14] Khalil. (2008). Simulation of nitrogen distribution in soil with drip irrigation system. *J. App. Sci.*, 8(18), 3157-3165. <https://dx.doi.org/10.3923/jas.2008.3157.3165>
- [15] Khan, J. N. et al. (2016). Simulation of mulch and no-mulch conditions for various soil matric potential thresholds for drip-fertigated Guava (*Psidium guajava* L.) in the semi-arid region of Northwest India. *J. of Irr. and Drain. Engg.*, 142(10), 1-15. [https://doi.org/10.1061/\(ASCE\)IR.1943-4774.0001047](https://doi.org/10.1061/(ASCE)IR.1943-4774.0001047)
- [16] Kurtzman, D., Shapira, R. H., Bar-Tal, A., Fine, P., & Russo, D. (2013). Nitrate fluxes to groundwater under citrus orchards in a Mediterranean climate: observations, calibrated models, simulations and agro-hydrological conclusions. *J. of Cont. Hyd.*, 15(1), 93-104. <https://doi.org/10.1016/j.jconhyd.2013.05.004>
- [17] Li, J., Zhang, J., & Rao, M. (2005). Modeling of water flow and nitrate transport under surface drip fertigation. *Trans. of the ASAE*, 48(2), 627-637. <https://doi.org/10.13031/2013.18336>
- [18] Li, S. X., Wang, Z. H., Li, S. Q., Gao, Y. J., & Tian, X. H. (2013). Effect of plastic sheet mulch, wheat straw mulch, and maize growth on water loss by evaporation in dryland areas of China. *Agrl. Water Manag.*, 116(1), 39-49. <https://doi.org/10.1016/j.agwat.2012.10.004>
- [19] Lubana, P. P. S., & Narda, N. K. (2001). SW-Soil and Water: Modeling soil and water dynamics under trickle emitters. *J. of Agrl. Engg. Res.*, 78(3), 217-232. <https://doi.org/10.1006/JAER.2000.0650>
- [20] Mostaghimi, S. J., Mitchell, K., & Lembke, W. D. (1982). Effect of discharge rate on distribution of moisture in heavy soils irrigated from a trickle source. *Trans. of the ASAE*, 25(4), 0975-0980. <https://doi.org/10.13031/2013.33649>
- [21] Phene, C. J., Davis, K. R., Hutmacher, R. B., & McCormick, R. L. (1987). Advantages of subsurface drip irrigation for processing tomatoes. *Acta Horti.*, 200(1), 101-113. <https://doi.org/10.17660/ActaHortic.1987.200.9>
- [22] Reddy, M. et al. (2012). Techno economic feasibility of drip irrigation for onion (*Allium cepa* L.). *Karnataka J. of Agrl. Sci.*, 25(4), 474-478. <http://14.139.155.167/test5/index.php/kjas/article/view/6652>
- [23] Rumpel, J. (2003). Effect of drip irrigation and fertilization timing and rate on yield of onion. *J. Veg. Crop Prod.*, 9(2), 65-73. [https://doi.org/10.1300/J068v09n02\\_08](https://doi.org/10.1300/J068v09n02_08)
- [24] Selim, T., Berndtsson, R., & Persson, M. (2013). Simulation of soil water and salinity distribution under surface drip irrigation. *Irr. and Drain.*, 62(3), 352-362. <https://doi.org/10.1002/ird.1739>
- [25] Selim, T. et al. (2018) Field experiment and numerical simulation of point source irrigation with multiple tracers. *Plos One*, 13(1), 1-15. <https://doi.org/10.1371/journal.pone.0190500>
- [26] Tameh, F., Asadollahfardi, G., & Darban, A. K. (2017). Mathematical model for reactive transport of heavy metals in soil column: based on PHREEQC and HP1 simulators. *Adv. in Envir. Res.*, 16(1), 67-81. <https://doi.org/10.12989/aer.2017.6.1.067>

# Empirical Measurement of Aesthetic Experience of Music

Abhishek Gupta\*<sup>1</sup> and C.M. Markan<sup>2</sup>

<sup>1</sup> Department of Cognitive Sciences,

<sup>2</sup> Department of Physics and Computer Science,  
Dayalbagh Educational Institute, Agra, 282007, Uttar Pradesh, India

*Chills or goosebumps, also called frisson, is a phenomenon that is often associated with an aesthetic experience e.g., music or some other ecstatic experience. The temporal and spatial cause of frisson in the brain has been one of the biggest mysteries of human nature. Accumulating evidence suggests that aesthetic, namely subjective, affective, and evaluative processes are at play while listening to music, hence, it is an important subjective stimulus for systematic investigation. Advances in neuroimaging and cognitive neuroscience, have given impetus to neuro-aesthetics, a novel approach to music providing a phenomenological brain-based framework for the aesthetic experience of music with the potential to open the scope for future research. In this paper, we present an affordable, wearable, easy-to-carry device to measure phenomenological goosebumps intensity on our skin with respect to real-time data using IoT devices (Raspberry pi 3, model B). To test the device subjects were asked to provide a list of songs that elicit goosebumps. Wireless earphones were provided, allowing participants to walk around and dance while listening to their music. (Some subjects moved during sessions). Results indicate that goosebumps were reliably detected by the device after visual inspection of the videos/music. The effective measurement when interfaced with neurophysiological devices such as electroencephalography (EEG) can help interpret biomarkers of ecstatic emotions. The second part of the study focuses on identifying primary brain regions involved in goosebump experience during musical stimulation.*

**Keywords** – Goosebumps, Frisson, Neuro-aesthetic, Neuroimaging, Electroencephalography, Ecstatic emotions

## I. INTRODUCTION

Music has the unique power to evoke moments of intense emotional and psychophysiological response. These moments known as 'chills', 'thrills', 'shockers', etc., are not only the subject of introspection and philosophical debate, but also of academic exploration of musical perception and perception in general. In the current article, we integrate existing interdisciplinary literature to define a comprehensive, testable, and ecologically valid model of transcendental psychophysiological moments in music. Music has a strong influence on people [1]. It improves memory, increases task endurance, improves mood, reduces anxiety and depression, prevents fatigue, improves pain response, and helps you exercise more effectively. Experience has three components: a subjective experience, a physiological response, and behavioral or expressive response. We experience emotions from birth and understand that something psychologically or biologically significant is affecting us. It is important to note that emotions influence not only behavior, but also objectively measurable physiological changes. An important physiological indicator [2] that has received a lot of attention is chills.

Aesthetic chills can be triggered by a variety of abstract and useful stimuli, including movies, poetry, and music. They are used to describe physiologically excited examples. It is also called 'arousal', 'stimulation', and 'tremor'. Under controlled conditions, this type of physiological arousal response is called hedonic or "arousal" (e.g., under laboratory conditions). Moreover, the eeriness of music is associated with dopamine production, which is associated with increased reward network activity. It is important to note that the musical chills as considered in this project often have physiological skin correlations in the form of goosebumps (i.e., emotional bristles, visible skin hairs) [3].

Goosebumps arise on the skin because of cold, fear, or pleasure, wherein small bumps appear on the skin surface because the hair turns out. As you might have observed, goosebumps tend to form when you're cold. In addition, they shape when you enjoy a sturdy emotional feeling, inclusive of extreme fear, sadness and pleasure. Goosebumps might also occur during instances of bodily exertion, even for small sports [4]. Goosebumps are a normal response but can also imply an underlying health situation.

This article is organized as follows. After the introduction in Section I, Section II describes how we developed the goosebump device. Section III describes the methodology

---

\*Corresponding author: [abhishekgupta215050@dei.ac.in](mailto:abhishekgupta215050@dei.ac.in)  
ISSN 0972-5032; Copyright ©2023, SSI

and evaluation tools used in this study. Section IV presents preliminary performance results using different feature selection methods. Section V describes the description and impact of this article. Section VI summarizes the work and mentions future work.

## II. EXPERIMENTAL SETUP

### A. Components of the device

The basic structure of the goosebump measuring device can be seen in Fig. 1. The structure is composed of an IoT (Internet of Things) device called Raspberry pi 3 Model B; a small camera fitted on the inside of the device (not shown in the figure) with white bands that help to bind the device with the subject's hand [6].

The devices work on the idea of comparing and analyzing images while setting a threshold value for certain attributes. The equipment basically takes images of the subject's skin during an experiment in which the subject listens to two kinds of music: favorite and unfavorable and our device recognizes the typical experience like goosebumps that appear as piloerections on the skin.



Fig.1. Representative picture of the goosebump measuring device fabricated in our lab. Parts of the device: raspberry pi settle on a black-colored stencil fitted with a camera on the inside (not shown in the picture) with white-colored straps to wear the device on hand.

### B. Installation of software tools

Raspbian software [7] was installed early in the process. A tool called Secure Shell (ssh) was added for security. The camera was then connected to the Raspberry Pi and paired using the MATLAB high-level programming language with all support packages. Subsequently, similar functional codes from previous studies [8] that were available on an open-source platform, were run in MATLAB for further experiments. Using a Raspberry Pi 3 as the base for the goosebump gadget opens a whole new variety of potential for students to innovate with this device concept [8]. For example, embedded microphones, skin conductance, and heart rate sensors, among many others, can be

easily attached to the Raspberry Pi and used to creatively utilize the device (e.g., to understand how heart rate could be related to musical goosebumps). To fully evaluate the device's potential, additional research is admittedly required. As we analyzed the Raspberry Pi's ability to detect the motion of hairs while goosebumps arise, the laptop showed live feeding of the camera, which shows a goosebump when the intensity of the goosebump exceeds the threshold level, making it possible to detect them [9].

## III. METHODOLOGY

We explored the idea of goosebumps in this paper and tested the results obtained from subjects. In the beginning, we asked some subjects about their favorite songs or videos that always give them goosebumps. Then, we put the device on their hand (Fig. 2) and played the desired song while continuously monitoring the intensity of goosebumps in MATLAB. Once a specific intensity of goosebumps appears, we spoke to the subjects about some of the songs we selected for them, and they also gave us goosebumps [10].



Fig. 2. A participant wearing a goosebump measuring device during experimentation in the lab.

Our device captures the skin images before the stimulus and after the stimulus is given. The terrain of the skin changes during an activity like piloerection or goosebumps (Fig. 3)



Fig. 3. Skin image grabbed by the device before (left) and during (right) goosebumps.

The electroencephalogram (EEG) is a test that analyses the electrical activity of the brain using tiny metal discs (electrodes) attached to the scalp. The next stage is to interface the device with the EEG. Even while you are asleep, electrical impulses are always being exchanged between brain cells. The primary goal of our investigation was to identify this activity (which can be seen as wavy lines in the EEG recording).

The participant was given a goosebumps device to hold while wearing a wet EEG cap with 64 electrodes (Fig. 4), and if goosebumps appeared, an automatic marking was made to make it easier to analyze the EEG results. While developing a marker, we took note of the duration and severity of the goosebumps and marked the ones that were longer than the threshold. We recorded EEG signals with various musical genres. Once the EEG data had been pre-processed, we analyzed the data in Brainstorm. Our software detects goosebumps and gives us the graph between the threshold value and the time (shown in Fig. 5).



Fig. 4. Subject wearing goosebumps measuring device with 64 channel wet EEG cap.

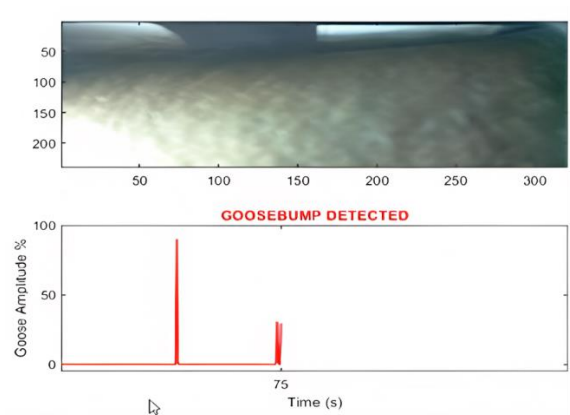


Fig. 5. Goosebumps detected in MATLAB. Graph peak corresponds to Fig. 3 (right) and flat to Fig. 3 (left)

#### IV. PRELIMINARY RESULTS

Firstly, from the data we got from the subjects without EEG, we found that the device was able to reliably detect most goosebumps experienced by the subject. After interfacing the device with 64-channel EEG we recorded the data on 30 subjects (these subjects were from different backgrounds and different academic and personal skills) and after that we analyzed it. Event Related Potential (ERP) and shell sphere method results showed similar patterns over all the subjects in our data. The Emotional responses centre of our brain is the prefrontal cortex [11].

On preliminary group analysis, we observed some similarity of activity in most of our subjects, specifically activity in the frontal region before goosebumps (Fig. 6a.) A type of combined activity is shown before the goosebump condition arises, during goosebumps (Fig. 6b.) a perfectly rated activity is shown in the pre-frontal cortex region of the brain, and after goosebumps (Fig. 6c.) the activity in the brain slows down. This activity needs to be further tested on a larger group of subjects through EEG/MEG.

Interestingly activity profiles bear a close similarity to the perception of beauty as detected experimentally using fMRI by Semir Zeki, a professor of neuro-aesthetics at University College London. According to him the mOFC, part of the reward and pleasure centers of the emotional brain, seems to light up when you're experiencing something beautiful [10].



Fig. 6a. Brain activity before goosebumps

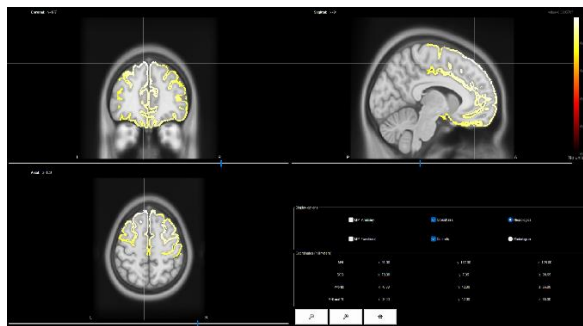


Fig. 6b. Brain activity during goosebumps

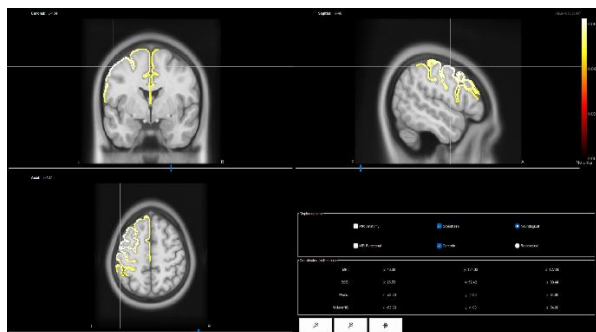


Fig. 6c. Brain activity after goosebumps

In another recent study [12], carried out using high-density EEG by Thibault Chabin a Ph.D. student at The University of Burgundy Franche-Comté in France also found that a specific activity over the prefrontal regions (e.g., bilateral insula, OFC, and SMA) increase in power when people get the chills from emotionally moving pieces of music.

## V. DISCUSSION AND IMPACT OF STUDY

There is a goosebumps device with the capability of measuring real-time goosebumps without movement affecting it. In contrast to previously created physiological recording and biofeedback systems based just on EDA, heart rate, a mix of the two, and even EEG signals, the device's ability to examine music-evoked emotion in real-world settings is a key feature [13]. It would be possible to study the connection between emotion and music learning in the classroom since kids, teens, and adults are better able to learn and perform in groups than as individuals. We also believe that a more advanced model of the device may have significant applications in the music industry because it adds an additional layer of quantifiable data that can enhance our impression of the music. As humans are naturally sociable beings, the device's biofeedback feature might allow us to express our feelings to other concertgoers and performers while dancing along to our favourite band's song without skipping a beat [14]. With the Pi 3 readily attached to the device, it can be utilized in creative ways because it has embedded microphones, skin conductance, heart rate, and other sensors. Further studies are necessary to gain a better comprehension of the device's potential.

## VI. CONCLUSION

The Raspberry Pi is a wearable sensor that measures goosebumps as an accurate physiological marker of musical emotions. It is necessary to refine the device and test it further in the future. During goosebumps, we saw certain patterns of activity on the frontal areas with EEG interfacing. Preliminary evidence suggests that the methodology is reliable when utilized by persons of diverse races and ethnicities, even though it should be resilient to variations in skin tone. We need to validate our findings through further research.

## REFERENCES

- [1] McCrae, R. R. (2007). Aesthetic chills as a universal marker of openness to experience. *Motivation and Emotion*, 31, 5–11. <https://doi.org/10.1007/s11031-007-9053-1>
- [2] Al-Nafjan, A., Hosny, M., Al-Ohali, Y., & Al-Wabil, A. (2017). Review and Classification of Emotion Recognition Based on EEG Brain-Computer Interface System Research: A Systematic Review. *Applied Sciences*, 7(12). <https://doi.org/10.3390/app7121239>
- [3] Ravaja, N., Saari, T., Salminen, M., Laarni, J., & Kallinen, K. (2006). Phasic Emotional Reactions to Video Game Events: A Psychophysiological Investigation. *Media Psychology*, 8, 343–367. [https://doi.org/10.1207/s1532785xmep0804\\_2](https://doi.org/10.1207/s1532785xmep0804_2)
- [4] Bajaj, V., & Pachori, R. B. (2015). Detection of Human Emotions Using Features Based on the Multiwavelet Transform of EEG Signals (A. E. Hassani and A. T. Azar, Eds.; Vol. 74, pp. 215–240). *Springer International Publishing*. [https://doi.org/10.1007/978-3-319-10978-7\\_8](https://doi.org/10.1007/978-3-319-10978-7_8)
- [5] Alakus, T. B., Gonen, M., & Turkoglu, I. (2020). Database for Emotion Recognition System Based on EEG Signals and Various Computer Games, *GAMEEMO*. 3. <https://doi.org/10.17632/b3pn4kwpmn.3>
- [6] Ghosh, L., Saha, S., & Konar, A. (2021). Decoding emotional changes of android-gamers using a fused Type-2 fuzzy deep neural network. *Computers in Human Behavior*, 116, 106640. <https://doi.org/10.1016/j.chb.2020.106640>
- [7] Pelofi, C., Goldstein, M., Bevilacqua, D., McPhee, M., Abrams, E., & Ripollés, P. (2021, June 1). CHILLER: A Computer Human Interface for the Live Labeling of Emotional Responses. *International Conference on New Interfaces for Musical Expression*. *NIME* 2021. <https://doi.org/10.21428/92fbeb44.5da1ca0b>
- [8] Bevilacqua, F., Engström, H., & Backlund, P. (2019). Game-Calibrated and User-Tailored Remote Detection of Stress and Boredom in Games. *Sensors*, 19(13). <https://doi.org/10.3390/s19132877>
- [9] Kivikangas, J. M. et al., (2011). A review of the use of psychophysiological methods in game research. *Journal of Gaming & Virtual Worlds*, 3, 181–199. [https://doi.org/10.1386/jgvw.3.3.181\\_1](https://doi.org/10.1386/jgvw.3.3.181_1)
- [10] Ishizu, T., & Zeki, S. (2011). Toward A Brain-Based Theory of Beauty. *PLOS ONE*, 6(7), e21852. <https://doi.org/10.1371/journal.pone.0021852>
- [11] Murugappan, M., Rizon, M., Nagarajan, R., Yaacob, S., Hazry, D., & Zunaidi, I. (2008). Time-Frequency Analysis of EEG Signals for Human Emotion Detection (N. A. Abu Osman, F. Ibrahim, W. A. B. Wan Abas, H. S. Abdul Rahman, & H.-N. Ting, Eds.; Vol. 21, pp. 262–265). *Springer Berlin Heidelberg*. [https://doi.org/10.1007/978-3-540-69139-6\\_68](https://doi.org/10.1007/978-3-540-69139-6_68)
- [12] Chabin, T. et al. (2020). Cortical Patterns of Pleasurable Musical Chills Revealed by High-Density EEG. *Frontiers in Neuroscience*, 14. <https://www.frontiersin.org/articles/10.3389/fnins.2020.565815>
- [13] Kim, J., & André, E. (2008). Emotion recognition based on physiological changes in music listening. *IEEE Transactions on Pattern Analysis and Machine Intelligence*, 30(12), 2067–2083. <https://doi.org/10.1109/TPAMI.2008.26>
- [14] The circumplex model of affect: An integrative approach to affective neuroscience, cognitive development, and psychopathology—PubMed. (n.d.). Retrieved February 12, 2023, from <https://pubmed.ncbi.nlm.nih.gov/16262989/>

# Role of Thermal Annealing in Fabrication of Bismuth Ferrite Thin Films for Photoelectrochemical Water Splitting

Bhanupriya\*, Kumari Ruchi, Runjhun Dutta, Anuradha Verma, Anupam Srivastav, Manju Srivastava and Rohit Shrivastav

Department of Chemistry,  
Dayalbagh Educational Institute, Agra, 282005, Uttar Pradesh, India

*This study deals with the preparation of perovskite-BiFeO<sub>3</sub> thin films annealed at different temperatures. Perovskite-BiFeO<sub>3</sub> has tendency to absorb visible portion of the solar spectrum, making it a suitable candidate to be used as photoelectrode for photoelectrochemical water splitting. The process adopted for synthesizing thin films was sol-gel spin coating. Polycrystalline nature with rhombohedral phase of thin films was identified by XRD analysis. Optical studies revealed absorption of perovskite-BiFeO<sub>3</sub> thin films in the visible region. The highest photocurrent density of 0.22 mA/cm<sup>2</sup> at 1 V vs SCE was obtained for thin films annealed at 700°C.*

**Keywords** – Annealing temperature, Perovskite, Polycrystalline thin films, Sol-gel spin coating

## I. INTRODUCTION

The worldwide demand for energy is constantly escalating with growing population and modernization. At the same time, the consumption of fossil fuels to cover the high energy demand is overloading our environment with carbon dioxide and greenhouse gases. As an adverse consequence of this, global warming has become one of the biggest problems of our time. Much of the energy required comes from the burning of fossil fuels. Since these non-renewable sources (fossil fuels) are limited and the dominance of these sources leads to environmental problems, researchers are looking for efficient and renewable energy sources to replace fossil fuels. This transition from non-renewable to renewable intensive energy production can provide a sustainable, clean, affordable, and long-lasting fuel for the future, i.e., it would bring both environmental and economic benefits.

Solar energy has the maximum global electricity generation capacity of more than 20 TW [1]. The solar energy can also be captured and converted into chemical energy and stored in the form of hydrogen. The hydrogen has high energy-to-weight ratio, high heat of combustion, and gives only water as a combustion product [2]. The photoelectrochemical (PEC) splitting of water is one of the environmental-friendly processes to produce hydrogen by fabricating suitable semiconductor photoelectrodes. To enhance the solar to hydrogen (STH) efficiency, it is needed to shift the absorption edge of the photoelectrode into the visible region which forms nearly 43% of the solar energy.

\*Corresponding author: [bhanupriya0227@gmail.com](mailto:bhanupriya0227@gmail.com)  
ISSN 0972-5032; Copyright ©2023, SSI

Perovskites, which are mixed oxides of transition metals, are recently being investigated as promising candidates for solar to hydrogen conversion by PEC route. BiFeO<sub>3</sub> (BFO) is a multiferroic material used in various applications such as data storage and magnetic sensors [3]. BFO has application in hydrogen production using photocatalytic and photoelectrochemical water splitting because of its narrow band gap (approx. 2.2 eV) and bulk photovoltaic properties [4], [5]. The narrow band gap allows absorption of visible light extending up to 750 nm [6]. Further, the depolarization of the electric field existing in BiFeO<sub>3</sub> based materials may reduce the recombination of the photo generated charge carriers during the transmission process and this may increase the quantum efficiency [7], [8].

In the present work, polycrystalline BFO thin films were prepared over the conducting glass substrate by sol-gel spin coating method. The method used for fabrication was simple and cost effective. The study focuses on the phase transition of the BFO material at different temperatures. The Bismuth nitrate and iron nitrate were used as precursors. The films were sintered at temperatures 700, 715 and 730 °C for one hour in a tubular furnace in air. The prepared films were further subjected to the characterization and PEC study.

## II. EXPERIMENTAL WORK

### A. Synthesis

The sol-gel spin coating was used to synthesize BFO thin films on the pre-cleaned conducting glass substrate. The precursors taken for synthesis are bismuth nitrate [Bi(NO<sub>3</sub>)<sub>3</sub> H<sub>2</sub>O] and iron nitrate [Fe(NO<sub>3</sub>)<sub>3</sub> H<sub>2</sub>O]. Bismuth

nitrate and iron nitrate were taken in the mole ratio of 1.05:1 and dissolved in the 2-methoxy ethanol solution. For the complete dissolution of the raw materials, a small amount of acetic acid was also added. The content was stirred for 12 hours [9]. This synthesis has been done at room temperature. Spin coating was performed at 3000 rpm for 20 s over the conducting glass substrate. After spin coating the wet films were dried. The deposited films were crystallized at different annealing temperatures of 700, 715 and 730 °C for 1 hour. One-third area of conductive substrate was covered with scotch tape during deposition of the thin films, to form an electrical contact later and photoelectrodes were fabricated for PEC analysis.

### B. Characterization

Phase analysis was done by X-ray Diffractometer (Bruker AXS D8 Advance, Germany) using the Cu-K $\alpha$  radiation ( $\lambda=1.54 \text{ \AA}$ ). The instrument was equipped with graphite monochromator and mirror at fixed incidence angle of 1-5°. The angular accuracy was 0.001° and the angular resolution was better than 0.01°. The analysis was made at  $2\theta$  ranging from 30 and 70° with scan speed of 2 s/step and increment of 0.02°. For crystal phase analysis, the obtained X-ray diffraction data was compared with JCPDS (Joint Committee on Powder Diffraction Standards) database. The observed X-ray diffraction data was also utilized to evaluate the average size of crystallites in the thin film samples. The estimations were based on the use of Scherrer's equation:

$$s = k \lambda / B \cos \theta \quad (1)$$

where  $k$  is a constant which equals to 0.9,  $\lambda$  the X-ray wavelength which equals to 0.154 nm,  $B$  is the full width at half maximum intensity,  $\theta$  the half diffraction angle and  $s$  gives particle size in nanometer [10].

Further, micro-strain ( $\gamma$ ) and dislocation density ( $\eta$ ) in the samples were also evaluated using (2) and (3).

$$\gamma = B (\cos \theta) / 4 \quad (2)$$

$$\eta = 1/s^2 \quad (3)$$

Optical characterization was done by using double beam UV-visible spectrophotometer (UV-2450, Shimadzu, Japan). The absorption was scanned in the range of 300-800 nm. Tauc plots between  $(\alpha h\nu)^2$  and photon energy ( $h\nu$ ) were obtained. Here,  $\alpha$ ,  $h\nu$  and  $E_g$  are absorption coefficient, photon energy and optical band gap, respectively.

$$(\alpha h\nu)^2 = C(h\nu - E_g) \quad (4)$$

The linear absorption edge of  $(\alpha h\nu)^2$  vs.  $h\nu$  plot, on extrapolation to the energy axis, yielded the band gap

energy values. Surface morphology of the prepared thin films was explored by recording images from scanning electron microscope (SEM, Carl Zeiss SUPRA 40 VP) at 15 kV accelerating voltage and ~4 mm working distance. Surface topography was investigated by atomic force microscopy, using Nanosurf easyscan Atomic Force Microscopy (AFM) unit (Version: 1.8, Switzerland) and the thickness was measured by surface profilometer (Tencor Alpha Step D-120).

Photoelectrochemical sensitivity of the thin films was studied by using Electrochemical Work Station (EWS, Model: PP211, CIMPS-pcs, Zahner, Germany). These thin films were fabricated to form photoelectrode. Experiments were performed using as-synthesized photoelectrodes as working electrode, platinum mesh as counter electrode, and saturated calomel electrode as reference electrode. A solution of 0.1 M NaOH (pH 13) was used as electrolyte throughout the measurements. All the physical and electrochemical characterization have been performed at the Department of Chemistry, Dayalbagh Educational Institute, Agra.

### III. RESULT AND DISCUSSION

X-Ray diffraction pattern of the prepared BFO thin films have been recorded in the  $2\theta$  range from 20° to 60° with a Bruker D8 Advance Diffractometer. The diffractogram for BFO is illustrated in Fig.1. The diffraction pattern showed that the peaks for BFO phase were there in all samples suggesting a polycrystalline nature with the rhombohedral structure. The peaks for BFO at  $2\theta$  values 32.09, 39.50 and 45.77 correspond to diffraction from (110), (111) and (200) planes respectively (JCPDS No- 010890510). It was observed that (110) peak of the film annealed at 730°C showed the highest intensity among all the samples, which indicated that the heat treatment at 730°C promoted the growth of (110) plane. The other phases might also appear during synthesis of BFO thin films due to the kinetics of phase formation but BiFeO<sub>3</sub> remains the major phase because of the fact that annealing in the air fills the vacancies that are created by bismuth volatilization [11]. The FWHM (full width half maximum) for the films annealed at 700, 715 and 730°C were calculated and had value of 0.44, 0.33 and 0.31 respectively, and the particle size calculated by Scherrer's equation found out to be 31, 40 and 44 nm, respectively. So, it was observed by the pattern that the intensity of peaks increases with increase in temperature, along with the decrease in the FWHM values indicating that the grain size has grown with respect to increase in annealing temperature. The samples prepared by varying annealing temperatures were analyzed by recording the SEM images. The analysis was intended to draw information regarding possible changes to the surface morphology with variation in sintering temperature. The BFO thin film annealed at 730 °C is denser than that at 715 °C and 700 °C and the grain size increases with the rise of annealing temperature. The observed SEM images of films are presented in Fig. 2(a)-(c).

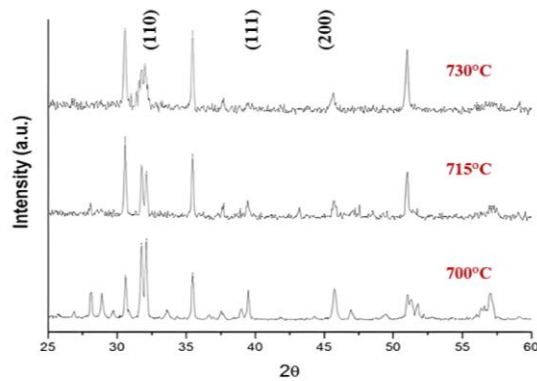


Fig. 1. XRD of thin films

TABLE I  
MICRO-STRUCTURAL DETAILS OF THIN FILMS SYNTHESIZED

Sintering Temperature	S (nm)	( $\gamma$ ) $\times 10^{-14}$	( $\eta$ ) $\times 10^{-3}$
700 °C	31	0.43	1.04
715 °C	40	0.33	0.62
730 °C	44	0.30	0.51

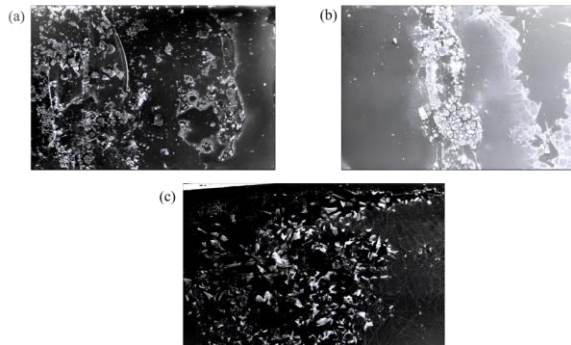


Fig. 2. SEM image of thin film sintered at 700°C (a), 715°C (b) and 730°C (c).

In order to assess the variation in surface topography, the films annealed at varying temperatures were subjected to AFM analysis. The observed AFM images of representative samples are presented in Fig. 3 (a)-(c). The roughness of the film increased with increase in sintering temperature due to increase in grain size. The thickness of the thin films was measured by surface profilometry and the average thickness of the thin films was obtained as 72 nm.

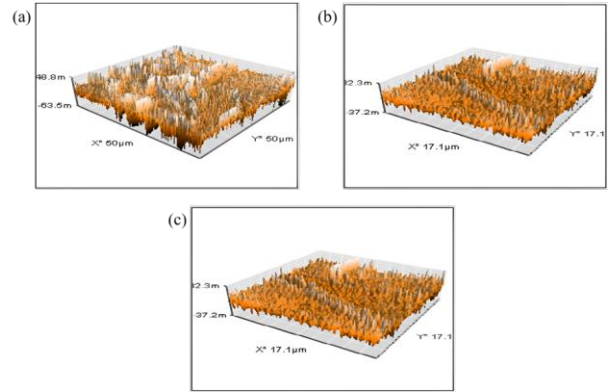


Fig. 3. AFM image of thin film sintered at 700°C (a), 715°C (b) and 730°C (c).

Optical characterization of thin films was done and observed absorption at different annealing temperatures are presented in Fig. 4. The absorption data was further utilized to obtain Tauc plots between  $(\alpha h\nu)^2$  and  $h\nu$  (Fig. 5). From the Tauc plots the direct band gap energy of samples was calculated. The average band gap of the thin films was around 2.3 eV and all the films absorb visible light of the solar spectrum.

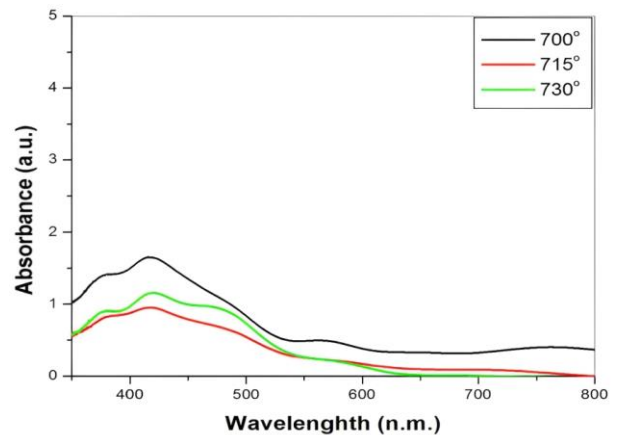


Fig. 4. Absorbance vs. wavelength plot

The photoelectrochemical performance of perovskite-BiFeO<sub>3</sub> photoelectrode towards water splitting was studied by observing the current- voltage (I-V) curve. The current-voltage curve confirmed the n-type conductivity of the BFO electrodes as photocurrent was observed under anodic bias. BFO thin film annealed at temperature 700°C exhibited the highest current density of 0.22 mA/cm<sup>2</sup> at 1 V/SCE, while the photocurrent density for thin films sintered at 715°C and 730°C were 0.15 mA/cm<sup>2</sup> and 0.05 mA/cm<sup>2</sup>, respectively, at 1 V/SCE. It was found that the photocurrent density decreases with increase in the annealing temperature.

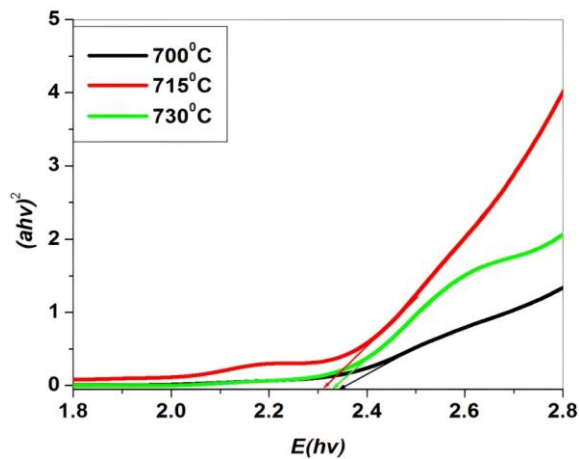


Fig. 5.  $(\alpha h\nu)^2$  vs  $h\nu$  plot of films sintered at different temperatures.

It is well known that perovskite-BiFeO<sub>3</sub> material shows remnant polarization which decreases with the rise in annealing temperature [12]. Therefore, photocurrent density observed in the BFO thin films which are annealed at 700°C seems to be intimately correlated with its high internal depolarization field caused by larger remnant polarization. It is believed that more effective separation of electron and holes takes place at the high depolarization field and this boosts the photocurrent density output.

Furthermore, the present work was compared with the work done in the literature and it was shown that the present method is simpler and more cost-effective to be adopted to synthesize BiFeO<sub>3</sub> in the future.

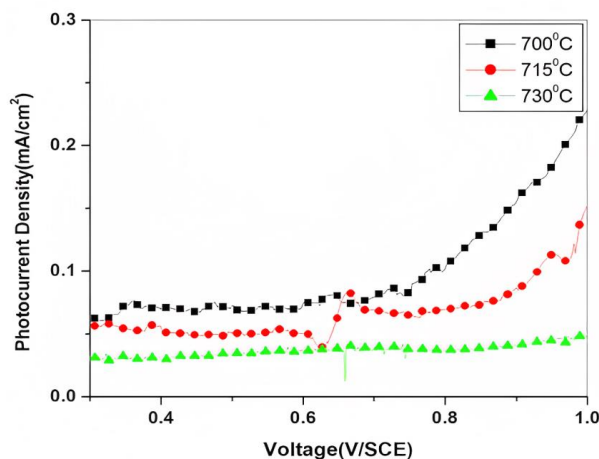


Fig. 6. Current- voltage curve for the BFO thin films annealed at different temperatures.

TABLE II  
COMPARISON OF THE STUDY WITH PREVIOUS WORKS

System	Preparation method	Photocurrent density	Reference
BiFeO <sub>3</sub>	Sol gel spin coating using acetic anhydride (hazardous)	0.14 mA/cm <sup>2</sup> at 1 V vs RHE	13
Y <sub>3+</sub> doped BiFeO <sub>3</sub>	Pulse Layer Deposition (costly technique)	0.72 mA/cm <sup>2</sup> at 1.4 V vs RHE	14
TiO <sub>2</sub> over-layer and CoOx	Atomic Layer Deposition and Electro-deposition	0.16 mA/cm <sup>2</sup> at 1.23 V vs RHE	15
Hydrogen treated BiFeO <sub>3</sub>	Drop-Casting Method	0.69 μA/cm <sup>2</sup> at 1.23 V vs Ag/AgCl	16
BiFeO <sub>3</sub>	Sol- gel Spin coating	0.22 mA/cm <sup>2</sup> at 1 V vs SCE	Present Work

#### IV. CONCLUSION

Pervoskite-BiFeO<sub>3</sub> thin films were prepared by sol-gel method and the effects of annealing temperatures on the structural, optical and photoelectrochemical properties have been investigated and the following conclusions can be drawn from the study and observations. Annealing temperature is a vital parameter which influences the growth of the BFO thin films. It not only effects the crystalline and microstructural properties, but even the optical and photoelectrochemical properties are also influenced. X-ray analysis showed that the BFO thin films have polycrystalline rhombohedral crystal structure, and the thin film annealed at 730 °C has high intensity peak with larger grain particles of average size 44 nm. So, it is clear that the intensity of peaks increases with increase in temperature, along with the decrease in the FWHM values indicating that the grain size might have grown with respect to increase in annealing temperature. PEC studies revealed maximum photocurrent density of 0.22 mA/cm<sup>2</sup> at 1 V/SCE at 700 °C as compared to values at 715 °C and 730 °C and it is due to gradual decrease in the remnant polarization at high temperatures, which creates less internal depolarization field. It leads to the low photocurrent density at higher temperatures due to less separation of the photo-generated charge carrier and high recombination rate. The band gap energy calculated from the Tauc plots comes out to be 2.3 eV, implying that the BFO thin films can absorb visible light which give advantage over other

typical ferroelectric materials like BaTiO<sub>3</sub> and SrTiO<sub>3</sub> based thin films that absorb UV light because of its larger band gap (>3 eV).

### ACKNOWLEDGMENTS

Financial support from Department of Science & Technology, Ministry of Science & Technology, Govt. of India under (DST/TMD/HFC/2K18/16(C)) research project and FIST Programme (CS-II/2017/38) is gratefully acknowledged. First author thanks University Grants Commission, Govt. of India, for the award of CSIR-UGC NET-JRF Fellowship.

### REFERENCES

- [1] Lewis, N.S. et al., Basic Research Needs for Solar Energy Utilization. Report of the Basic Energy Sciences Workshop on Solar Energy Utilization, April 18-21, 2005. United States. <https://doi.org/10.2172/899136>
- [2] Vijayaraghavan, K., & Mohd Amin Mohd Soom, (2006). Trends in biohydrogen generation – A review. *Environmental Sciences*, 3(4), 255-271. <https://doi.org/10.1080/15693430601049660>
- [3] Baloni, M. et al., (2022). Enhanced multiferroic properties and magnetoelectric coupling in Nd modified 0.7BiFeO<sub>3</sub>-0.3PbTiO<sub>3</sub> solid solution. *Journal of Materials Science: Materials in Electronics*, 33 (21), 17161-17173. <https://doi.org/10.1007/s10854-022-08592-0>
- [4] Heo, Y., & Alexe, M. (2021). Boosting Piezoelectricity under Illumination via the Bulk Photovoltaic Effect and the Schottky Barrier Effect in BiFeO<sub>3</sub>. *Advanced Materials*, 34(5), 210584. <https://doi.org/10.1002/adma.202105845>
- [5] Glück, N., & Bein, T. (2020). Prospects of lead-free perovskite-inspired materials for photovoltaic applications. *Energy & Environmental Science*, 13(12), 4691-4716. <https://doi.org/10.1039/D0EE01651A>
- [6] Deng, J., Banerjee, S., Mohapatra, S.K., & Smith, Y.R. (2011). Bismuth Iron Oxide Nanoparticles as Photocatalyst for Solar Hydrogen Generation from Water. *Journal of Fundamentals of Renewable Energy and Applications*, 1. doi:10.4303/jfrea/R101204
- [7] Brody, P.S. (1973). Large polarization-dependent photovoltages in ceramic BaTiO<sub>3</sub> + 5 wt. % CaTiO<sub>3</sub>. *Solid State Communication*, 12, 673-676. [https://doi.org/10.1016/0038-1098\(73\)90310-4](https://doi.org/10.1016/0038-1098(73)90310-4)
- [8] Qin, M., Yao, K., Liang, Y. C., & Shannigrahi, S. (2007). Thickness effects on photoinduced current in ferroelectric (Pb 0.97 La 0.03) (Zr 0.52 Ti 0.48) O 3 thin films. *Journal of Applied Physics*, 101(1), 014104. <https://doi.org/10.1063/1.2405732>
- [9] Ren, Y., Zhu, X., Zhang, C., Zhu, J., Zhu, J. & Xiao, D. (2014). High stable dielectric permittivity and low dielectric loss in sol-gel derived BiFeO<sub>3</sub> thin films. *Ceramics International*, 40(1), 2489-2493. <https://doi.org/10.1016/j.ceramint.2013.07.051>
- [10] Kaur, G., Khan, S.A., Satsangi, V.R., Dass, S. & Shrivastav, R. (2021). Nano-hetero-structured thin films, ZnO/Ag-(α) Fe<sub>2</sub>O<sub>3</sub>, with n/n junction, as efficient photoanode for renewable hydrogen generation via photoelectrochemical water splitting. *Renewable Energy*, 164, 156-170. <https://doi.org/10.1016/j.renene.2020.09.060>
- [11] Tabares-muñoz, C., Rivera, J.P. and Schmid, H. (1984). Ferroelectric domains, birefringence and absorption of single crystals of BiFeO<sub>3</sub>. *Ferroelectrics*, 55(1), 235-238. <https://doi.org/10.1080/00150198408015377>
- [12] Zhang, Y. et al., (2020). Enhanced photovoltaic properties of gradient calcium-doped BiFeO<sub>3</sub> films. *Ceramics International*, 46(8), 10083-10088. <https://doi.org/10.1016/j.ceramint.2019.12.276>
- [13] Albagle, F. (2017). Synthesis of Bismuth Ferrite for Photoelectrochemical Water Splitting. Graduate Theses, Dissertations, and Problem Reports. 5050. <https://researchrepository.wvu.edu/etd/5050>
- [14] Haydous, F. et al., (2018). Rolling dopant and strain in Y-doped BiFeO<sub>3</sub> epitaxial thin films for photoelectrochemical water splitting. *Scientific reports*, 8(1), 1-11. <https://doi.org/10.1038/s41598-018-34010-9>
- [15] Liu, G. et al., (2020). Enhancement of the photoelectron-chemical water splitting by perovskite BiFeO<sub>3</sub> via interfacial engineering. *Solar Energy*, 202, 198-203. <https://doi.org/10.1016/j.solener.2020.03.117>
- [16] Zhang, C., Li, Y., Chu, M., Rong, N., Xiao, P. & Zhang, Y. (2016). Hydrogen-treated BiFeO<sub>3</sub> nanoparticles with enhanced photoelectrochemical performance. *RSC advances*, 6(29), 24760-24767. <https://doi.org/10.1039/C5RA23699A>

# Comparative Analysis of Fine Particulate Matter (PM<sub>2.5</sub>) over the Indo-Gangetic Plain (IGP) in the Era of Covid-19: Normal to the New Normal

Isha Goyal, Muskan Agarwal, Simran Bamola, K. Maharaj Kumari and Anita Lakhani\*

Department of Chemistry  
Dayalbagh Educational Institute, Agra, 282005, Uttar Pradesh, India

*The world is still shadowed by the COVID-19 pandemic. Many countries have implemented mitigation and control strategies to minimize the outbreak of this pandemic disease. As governments around the world were battling to manage COVID-19 outbreaks in the year 2020, the Government of India (GoI) implemented a strict lockdown policy to restrict the mobility of 1.3 billion people and control the spread of COVID-19. Lockdown, on the other hand, leads to significant changes in air quality trends as a result of reduced traffic activity and restricted human mobility. In this study, the air quality data of seven cities namely Agra (A), Noida (N), Faridabad (F), Kanpur (K), Lucknow (L), Ghaziabad (G) and Delhi (D) over the Indo Gangetic Plain (IGP) were used to compare the air quality in the era of COVID-19 from normal (2019) to "New Normal" (2021). During the year 2020, air quality improved, as compared to the year 2019 and year 2021. The maximum annual decrease of PM<sub>2.5</sub> was observed at N (17%) followed by G (14%), D (11%), F (8%), K (8%) and L (4%), whereas the slight increase was observed at A (9%) in the year 2020. Changes in PM<sub>2.5</sub> were also compared from 2020 to 2021, and a noticeable increase in PM<sub>2.5</sub> levels was found throughout 2021. The maximum improvement in the air quality index (AQI) was noticed at N (24%) and minimum at F and L (3% each) in 2020, while it suddenly rises by 12% at D in 2021, indicating that air quality returned back to its prior levels when the epidemic control measures were discontinued. Although the COVID-19 pandemic had severe negative consequences for human health and the world economy, likely, the reduction in air pollution and significant improvement in ambient air quality as a result of lockdowns brought major short-term health advantages. During the new normal, the government must develop regulations to control environmental challenges that are creating poor air quality.*

**Keywords** – AQI, Era of COVID-19 Pandemic, Indo-Gangetic Plain (IGP), New Normal (unrestricted period).

## I. INTRODUCTION

In the present and the ensuing decades, climate change and air pollution are major environmental concerns [1]. The quality of the air has significantly declined over the past few decades as a result of rising anthropogenic emissions, particularly in the Northern Hemisphere. Although the new Corona Virus (COVID-19) began to spread around the world at the end of 2019, many countries gradually implemented lockdown measures [2]. Epidemic control measures restricted human activities [3] and improved air quality from the previous levels (2019) overall, but the air quality in some cities showed a negative impact [3], and the air quality returned back to its prior levels when the epidemic control measures were discontinued [4]. Thus, epidemic prevention and control provided society with a good to opportunity observe the relationship between human activities and air quality, review past atmospheric environmental protection measures, and plan

better future atmospheric strategies. Lockdown during COVID-19 caused various changes in air quality around the world, and many researchers emphasized such changes in their studies [5]–[9]. The air-quality monitoring data was studied from 2019 to 2021 to assess the characteristics of the temporal and spatial distribution to study the influence of the rigorous control measures of the new COVID-19 epidemic on the air quality of Hubei in early 2020. During the active COVID-19 period, all air-quality pollutants were reduced, with a maximum decrease of 26% reported in PM<sub>10</sub>, 23% in PM<sub>2.5</sub>, and a minimum decrease of 5% in O<sub>3</sub>. Additionally, changes in air pollutants from 2017 to 2021 were compared, and it was shown that all pollutants decreased until the year 2020. Henceforth, the air quality index (AQI) showed a 2% post-COVID-19 increase, indicating that the quality of the air will deteriorate in the future, but a decrease of 22% was also observed during the active COVID-19 period [4]. Before and after COVID-19, Stefan Drews et al. highlighted the acceptance of climate change policies [10]. Ching and Kajino reconsidered the COVID-19 pandemic's impact on air quality from the context of the climate [11]. Zang et al., conducted a meta-analysis on the association of ambient air pollution and COVID-19 risk, to encourage the

\*Corresponding author: [anita.lakhani01@gmail.com](mailto:anita.lakhani01@gmail.com)

ISSN 0972-5032; Copyright ©2023, SSI

decision-makers to develop more effective prevention and control strategies for this unprecedented pandemic [12]. Shukla et al. documented the appraisal of the COVID-19 lockdown and unlocking effects on the air quality of North India. They observed that the beginning of anthropogenic activities significantly exceeded the changes in air quality during the COVID-19 lockdown during the various phases of unlocking [13]. The post-lockdown AQI values of 314 significant Chinese cities were studied by Feng et al., to compare their various effects on the determinants of urban resilience. They observed that after the closure, there was a reduction in air pollution emissions, and after the recession period, urban air quality returned to its prior levels. Divergent response patterns show different sensitivity levels of urban resistance to air pollution [14]. The air quality during the COVID-19 lockdown gathered the attention of researchers across the globe ([4], [15]–[18]), but none of the studies has attempted to analyze the status of air pollution post-COVID-19 lockdown in Indo Gangetic Plain (IGP). In the present study, a comparison of air quality of seven cities, namely Agra (A), Noida (N), Faridabad (F), Kanpur (K), Lucknow (L), Ghaziabad (G), and Delhi (D), located in the IGP (Fig. 1), was made in the era of COVID-19 from normal (2019) to "New Normal" (2021). According to the World Air Quality Report, IQ Air 2020 these cities have been identified as highly polluted cities in India [5]. This research aimed to increase understanding of the shifting patterns of air quality in each city prior to COVID-19, during COVID-19, and post-COVID-19.

## II. METHODOLOGY

### A. Study area

The study was carried out across the Indo-Gangetic Plain of India. The Indo-Gangetic Plain, also known as the North Indian River Plain, is a 700-thousand km<sup>2</sup> (172-million-acre) fertile plain encompassing northern regions of the Indian subcontinent, comprising the states of Punjab, Haryana, Delhi, Uttar Pradesh (U.P.), Bihar and West Bengal. The air quality monitoring data of seven cities Agra (A), Noida (N), Faridabad (F), Kanpur (K), Lucknow (L), Ghaziabad (G), and Delhi (D), were analyzed (Fig 1). Detailed information about these air quality monitoring stations is given in Table I. The latitudes and longitudes of

the study sites have been taken from (<https://www.wikipedia.org/>) and the population is taken from (<https://www.census2011.co.in/city.php>) as per 2011 census.

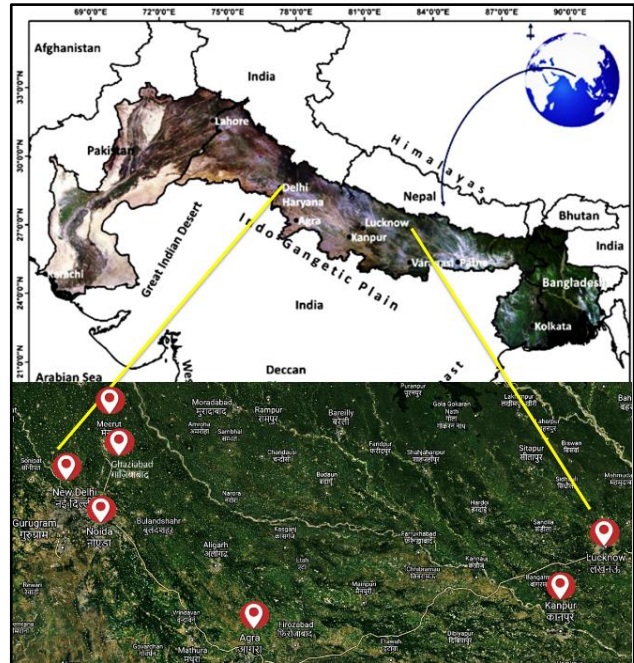


Fig 1. Study site

### B. Data collection

In this study, the data has been collected from the dashboard of Continuous Ambient Air Quality Monitoring system (CAAQM) regulated by Central Pollution Control Board (CPCB) over the seven monitoring sites spread across IGP (<https://app.cpcbcr.com/ccr/#/caaqm-dashboard-all/caaqm-landing>) (Table I). The data of PM<sub>2.5</sub>, has been collected from 1st January 2019 to 31st December 2021 to compare the air quality in the era of COVID-19 from normal (2019) to "New Normal" (2021).

TABLE I  
DESCRIPTION OF STUDY SITES

Sites/States	Location	Site Description	Managed by
Agra (A), Uttar Pradesh	27.10°N, 78.05°E	Sanjay Place <sup>a</sup>	CPCB
Faridabad (F), Haryana	28.25°N, 77.22°E	Sector 16 A <sup>a</sup>	HSPCB
New Delhi (D), Delhi	28.38°N, 77.12°E	Anand Vihar <sup>b</sup>	DPCC

Kanpur (K), Uttar Pradesh	26.28°N, 80.24°E	Nehru Nagar <sup>b</sup>	UPPCB
Noida (N), Uttar Pradesh	28.33°N, 77.37°E	Sector 125 <sup>b</sup>	UPPCB
Lucknow (L), Uttar Pradesh	26.55°N, 80.59°E	Talkatora District Industries Centre <sup>b</sup>	CPCB
Ghaziabad (G), Uttar Pradesh	28.40°N, 77.28°E	Vasundhara <sup>b</sup>	UPPCB

<sup>a</sup>Commercial Site, <sup>b</sup>Industrial Site

The monitored data with significant time resolution of one hour frequency was analysed. The concentrations at a sampling site were recorded with the standard deviation of less than 5% of the mean as having erroneous data (blank data points), and thus are not considered. Missing records, incorrect data (when  $PM_{2.5} > PM_{10}$ ), and outliers (abrupt increase in the typical patterned values) in the observation were excluded from the study because they were considered as invalid data. During the analysis period, sites with more than 60% valid data were explored for the study. Central Pollution Control Board (CPCB) provides quality assurance and data quality after following rigorous protocol, for the sampling, analysis and calibration, which is ensured as per the standards set by CPCB, India (<https://cpcb.nic.in/quality-assurance-quality-control/>). AQI values were also computed for the 24-h average of  $PM_{2.5}$  levels using the USEPA standard formula from the AirNow web portal (U.S. EPA, 1999).

### C. Statistical analysis

Statistical analysis was carried out using IBM SPSS 16.0 (IBM, USA). The main statistical test employed was the independent samples t-test. Comparisons between the two years were carried out by applying t-test at a significance level of 0.05.

## III. RESULTS AND DISCUSSION

### A. City-wise annual concentrations of $PM_{2.5}$ and AQI

The annual average of  $PM_{2.5}$  and air quality index (AQI) over the IGP from year 2019 to year 2021 were compared to better evaluate the impact of the changes on air quality patterns (Table II). The annual average concentration of  $PM_{2.5}$  was highest at D ( $128 \pm 105 \mu g m^{-3}$ ) followed by G ( $123 \pm 105 \mu g m^{-3}$ ), L ( $122 \pm 72 \mu g m^{-3}$ ), N ( $114 \pm 92 \mu g m^{-3}$ ), F ( $99 \pm 100 \mu g m^{-3}$ ), K ( $96 \pm 81 \mu g m^{-3}$ ) and A ( $73 \pm 49 \mu g m^{-3}$ ) in the year 2019. Similar trend with the inverted array between G and L was observed in the year 2020 (Table II). It was also noticed that the annual average of  $PM_{2.5}$ , at all the stations witnessed a significant reduction during this year due to the lockdown implemented [19]. In the year 2021, the annual average of  $PM_{2.5}$ , exhibited a progressively increasing trend with highest concentration at D ( $122 \pm 89 \mu g m^{-3}$ ) and lowest at A ( $79 \pm 63 \mu g m^{-3}$ ), indicating the air quality returned back to its prior levels when the epidemic control measures were discontinued [4]. Throughout all three years, PM concentrations exceeded the permissible limit of National Ambient Air Quality Standards, India ( $40.0 \mu g m^{-3}$ ; annual limit). This status of  $PM_{2.5}$  concentrations clearly states the health hazards to which the habita-

TABLE II  
ANNUAL CONCENTRATIONS OF  $PM_{2.5}$  AND AQI

Sites	$PM_{2.5}$			Number of days having unhealthy AQI by USEPA		
	Year 2019	Year 2020	Year 2021	Year 2019	Year 2020	Year 2021
Agra	73±49	80±58	79±63	315	276	303
Faridabad	99±100	91±85	102±90	278	269	288
Delhi	128±105	114±100	122±89	326	280	314
Kanpur	96±81	81±88	82±70	274	242	236
Noida	114±92	94±83	96±83	307	234	226
Lucknow	122±72	117±85	104±71	345	335	288
Ghaziabad	123±105	105±88	113±93	314	281	279

Data Source: CPCB

nts have been exposed. The AQI revealed that air quality in these cities were mainly distributed in unhealthy (76-95%) and moderate (5-20%) category in the year 2019. The air quality improved significantly ( $p < 0.05$ ) during the year 2020, as the unhealthy category was reduced (66-91%), while the moderate category (7-30%) was extended, indicating the impact of lockdown in the year 2020 [20]. However, air quality restored to pre-epidemic levels, i.e., unhealthy (68-92%) and moderate (8-20%) category in the year 2021, when the epidemic control measures were abandoned.

**B. City-wise relative change of  $PM_{2.5}$  and AQI**

The city-wise percentage change in average pollutant levels from the previous year is also depicted in Fig 2. The percentage decrease in the concentrations of  $PM_{2.5}$  during the year 2020 with respect to year 2019 was found maximum at N (17.2%) and minimum at L (3.9%), however, a significant increase ( $p < 0.05$ ) was observed at A (9.2%) in the same period [16]. This emphatic improvement in PM levels can be linked to a considerable reduction in road transportation, a pause in construction works, and industrial shutdown [4], [15], [21]. Moreover, a substantial percentage increase from year 2020 to year 2021 in the PM levels was observed for F (11.6%), D (6.8%), N (1.7%) and G (7.3%) among the explored cities in this study. The re-opening of industrial enterprises, automobile mobilization probably contributed to the elevated levels of  $PM_{2.5}$  during the year 2021 [13].

A remarkable improvement in AQI was also observed over IGP in the year 2020, compared to the previous year (2019) and after COVID-19 (2021). In the year 2019, each city had AQI within unhealthy for sensitive groups (101–150) and unhealthy (151–200) range according to US EPA standards. Conversely, the AQI levels improved by 4-13% in the year 2020 at the selected sites, which levelled off (3-11%) to pre-epidemic levels in 2021 as compared to the year 2020 (Fig 2).

**C. Comparison of  $PM_{2.5}$  concentrations during active period of COVID-19 with the same period of year 2019 and the year 2021**

The pre-COVID and post-COVID increase in pollutants have a variety of causes, including inadequate infrastructure in all regions of the selected sites, massive use of automobiles, a lack of vegetation, bare ground and human

activities. Additionally, several weather phenomena, such as haze, smog and fog, also have an impact on the air quality of the relevant places [4]. It is clearly observed that concentrations of  $PM_{2.5}$  was substantially reduced during active months of COVID-19, i.e., March, April and May (from 25<sup>th</sup> March, 2020 to 31<sup>st</sup> May, 2020) in the year 2020, in comparison to the same period of year 2019 and the year 2021 (Fig 3).

A substantial decrease in concentration of  $PM_{2.5}$  was observed in the month of March (18-84%) with maximum improvement at Faridabad, followed by May (1-68%) and April (18-61%) in the year 2020. The probable reason of the observed trend may be the migrant’s movement [22]. However, a considerable increase was observed in the month of March at Agra (523%), followed by Faridabad (394%) and Noida (381%) in the year 2021. The changes in  $PM_{2.5}$  levels, from 2019 to 2021, revealed that the air quality was restored to the prior levels of unhealthy air, after the restrictions were discontinued to re-establish the New Normal.

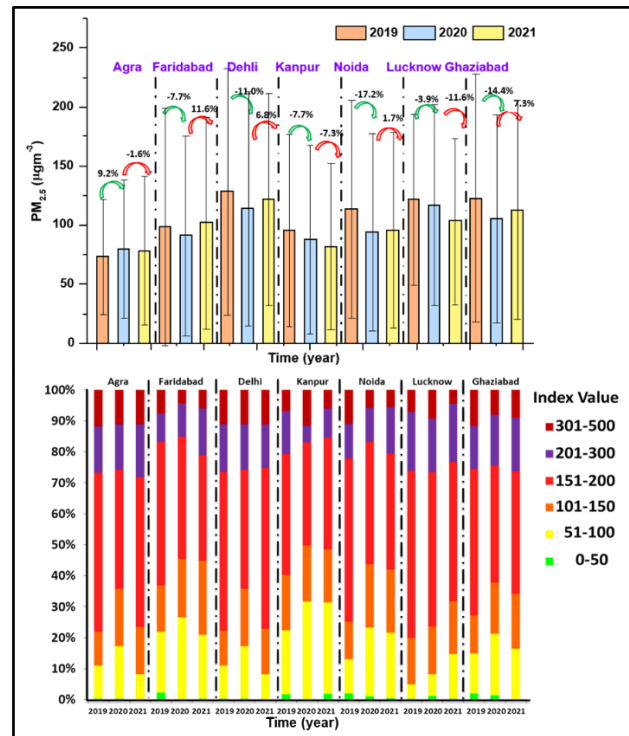


**Fig 2. City-wise daily changes in air quality patterns. In upper panel: the green arrow shows percentage changes from year 2019 to year 2020, whereas red arrow shows percentage changes from year 2020 to year 2021. In lower panel: the change in AQI levels was shown from year 2019 to year 2021.**

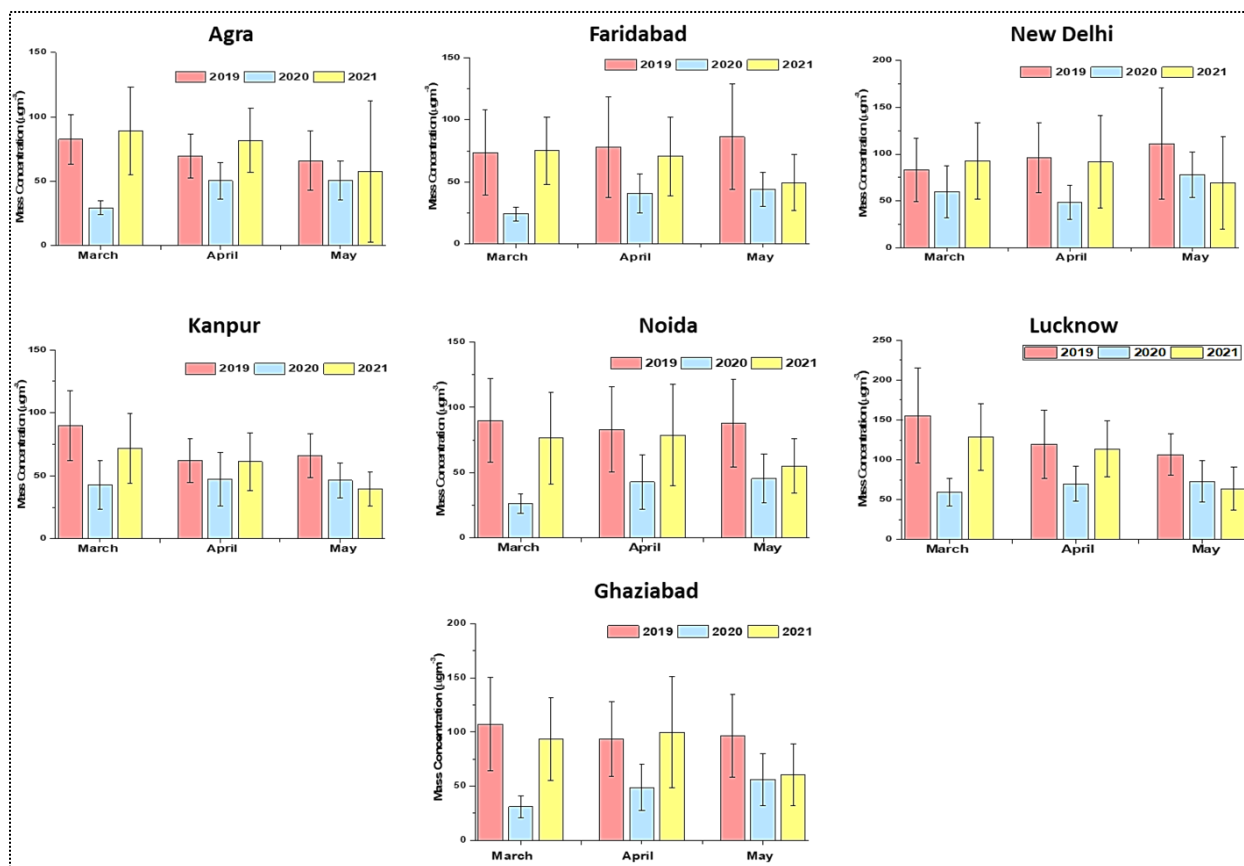


Fig 3. PM<sub>2.5</sub> concentrations during active period of COVID-19 and the same period observed in the year 2019 and the year 2021

#### IV. CONCLUSION

According to this study, there was a different degree of improvement in the annual average of PM<sub>2.5</sub> and AQI in the year 2020 over IGP compared to the year 2019 and 2021. A substantial decrease in concentration of PM<sub>2.5</sub> was observed in the month of March (18-84%), during the active-COVID-19 period, with a maximum improvement at Faridabad, followed by May (1-68%) and April (18-61%) in the year 2020. Conversely, a considerable increase in PM<sub>2.5</sub> was also observed in the month of March, 2021 at Agra (523%), followed by Faridabad (394%) and Noida (381%). However, in 2021, air pollution began to increase. The study suggests that, while the COVID-19 pandemic had numerous negative consequences for both human health and the global economy in the year 2020, lockdowns are likely to have had a significant positive influence on short-term health due to the reduction in air pollution and improvement in ambient air quality. Conversely, during the New Normal, poor air quality is caused by environmental issues that restore to its previous levels. According to the findings of the study, politicians and the private sector must undertake collective efforts to reduce atmospheric pollution and even population density in

cities, and the government must create rules to solve environmental concerns in order to re-attain the improved New Normal.

#### ACKNOWLEDGEMENTS

Authors are grateful to the Director, Dayalbagh Educational Institute and Head, Department of Chemistry for providing necessary facilities. The authors also thank to Central Pollution Control Board (CPCB), India for online data servers during this study period.

This work was supported by Department of Science and Technology (EMR/2017/002648) and Department of Science and Technology - Fund for Improvement of S&T Infrastructure (SR/FST/CS-II/2017/38).

#### REFERENCES

- [1] Von Schneidmesser, E. et al. (2015). Chemistry and the linkages between air quality and climate change. *Chemical reviews*, 115(10), 3856-3897.

- [2] Kondragunta, S., Wei, Z., McDonald, B. C., Goldberg, D. L., & Tong, D. Q. (2021). COVID-19 induced fingerprints of a new normal urban air quality in the United States. *Journal of Geophysical Research: Atmospheres*, 126(17), e2021JD034797.
- [3] Mahato, S., & Ghosh, K. G. (2020). Short-term exposure to ambient air quality of the most polluted Indian cities due to lockdown amid SARS-CoV-2. *Environmental Research*, 188, 109835.
- [4] Aamir, M. et al. (2021). Spatiotemporal change of air-quality patterns in Hubei province—a pre- to post-COVID-19 analysis using path analysis and regression. *Atmosphere*, 12(10), 1338.
- [5] Air, I. Q. (2020). 2019 World Air Quality Report.
- [6] Srivastava, S., Kumar, A., Baudhh, K., Gautam, A. S., & Kumar, S. (2020). 21-day lockdown in India dramatically reduced air pollution indices in Lucknow and New Delhi, India. *Bulletin of environmental contamination and toxicology*, 105, 9-17.
- [7] Dey, T., & Dominici, F. (2020). COVID-19, air pollution, and racial inequity: connecting the dots. *Chemical Research in Toxicology*, 34(3), 669-671.
- [8] Suman, R. et al. (2021). Impact of COVID-19 Pandemic on Particulate Matter (PM) concentration and harmful gaseous components on Indian metros. *Sustainable Operations and Computers*, 2, 1-11.
- [9] He, G., Pan, Y., & Tanaka, T. (2020). The short-term impacts of COVID-19 lockdown on urban air pollution in China. *Nature sustainability*, 3(12), 1005-1011.
- [10] Drews, S., Savin, I., & van den Bergh, J. (2022). Climate change concern and policy support before and after COVID-19. *Ecological Economics*, 199, 107507.
- [11] Ching, J., & Kajino, M. (2020). Rethinking air quality and climate change after COVID-19. *International Journal of Environmental Research and Public Health*, 17(14), 5167.
- [12] Zang, S. T., et al. (2022). Ambient air pollution and COVID-19 risk: evidence from 35 observational studies. *Environmental research*, 204, 112065.
- [13] Shukla, S., Khan, R., Saxena, A., Sekar, S., Ali, E. F., & Shaheen, S. M. (2022). Appraisal of COVID-19 lockdown and unlocking effects on the air quality of North India. *Environmental Research*, 204, 112107.
- [14] Feng, M., Ren, J., He, J., Chan, F. K. S., & Wu, C. (2022). Potency of the pandemic on air quality: An urban resilience perspective. *Science of The Total Environment*, 805, 150248.
- [15] Lokhandwala, S., & Gautam, P. (2020). Indirect impact of COVID-19 on environment: A brief study in Indian context. *Environmental research*, 188, 109807.
- [16] Kumari, S., Lakhani, A., & Kumari, K. M. (2020). COVID-19 and air pollution in Indian cities: World's most polluted cities. *Aerosol and Air Quality Research*, 20(12), 2592-2603.
- [17] Mor, S., Kumar, S., Singh, T., Dogra, S., Pandey, V., & Ravindra, K. (2021). Impact of COVID-19 lockdown on air quality in Chandigarh, India: understanding the emission sources during controlled anthropogenic activities. *Chemosphere*, 263, 127978.
- [18] CPCB, "IMPACT OF LOCKDOWN (25th March to 15th April) ON AIR QUALITY "IMPACT OF JANTA CURFEW & LOCKDOWN", 2020. Online Available: <http://www.indiaenvironmentportal.org.in/files/file/Impact-Of-Lockdown-On-Air-Quality.pdf>
- [19] Sahoo, P. K. et al. (2021). Pre-to-post lockdown impact on air quality and the role of environmental factors in spreading the COVID-19 cases-a study from a worst-hit state of India. *International journal of biometeorology*, 65, 205-222.
- [20] Sathe, Y., Gupta, P., Bawase, M., Lamsal, L., Patadia, F., & Thipse, S. (2021). Surface and satellite observations of air pollution in India during COVID-19 lockdown: Implication to air quality. *Sustainable cities and society*, 66, 102688.
- [21] Yadav, R. et al. (2020). COVID-19 lockdown and air quality of SAFAR-India metro cities. *Urban Climate*, 34, 100729.
- [22] Manchanda, C. et al. (2021). Variation in chemical composition and sources of PM<sub>2.5</sub> during the COVID-19 lockdown in Delhi. *Environment International*, 153, 106541.

# Prosthetics Advice, Design and Fabrication using Digital Manufacturing Systems for Improved Healthcare Systems

Guru Ratan Satsangee\*, Bobby Tyagi, Dheeraj Kumar Angajala, Ankit Sahai and Rahul Swarup Sharma

Department of Mechanical Engineering,  
Dayalbagh Educational Institute, Agra, 282005, Uttar Pradesh, India

*Recent surveys show that about one million Indians are living with amputations. Amputation is the removal of all or part of a limb or extremity due to trauma, surgery, or medical illness. Prostheses play a crucial role in making the amputees mobile. As each patient and their amputation is unique, each prosthetic limb should be customised to their requirements. Designing and fabrication of customised prosthesis is a long process involving meticulous measurement and rounds of consultation by prosthetists with the patient/client. As customised designing and fabrication of prosthesis is a costly affair, many amputees have to do with the standardized prosthetic limbs. In view of this need, a project was initiated at DEI in which our team visited a medical camp and identified 'getting the perfect fit' as a major problem for amputees. This paper is an attempt to showcase how this problem can be solved by using technologies of high-resolution scanners, CAD and 3-D printing.*

**Keywords** – 3D printing, 3D scanning, Additive manufacturing, Prosthetics, CAD/CAM, Digital manufacturing.

## I. INTRODUCTION

Limb loss, also known as amputation, is an event of removal of a limb due to trauma, surgery, or medical illness. This event can be physically as well as psychologically challenging for any person specially to access equal opportunities under many circumstances [1]. Mobility assistive devices like prostheses plays a vital role in making amputees mobile. Amputation is a significant issue in the healthcare system of our country. There are around one million amputees in India, and approximately 23,500 new amputations are recorded annually [2]. Most of these people rarely get any rehabilitation support from the government due to the country's large informal sector. Further, more than two-thirds of India's population lives in rural areas with limited financial and healthcare accessibility [3]. This section of the population is most affected by accidents due to unsafe working conditions resulting in limb loss.

The lack of prosthetic facilities not only has a physical impact on the individual but also poses a significant challenge to the nation [4]. Providing high-quality, affordable prosthetic service is critical for ensuring independence and social integration of physically unique people. A functional prosthetic device will help them gain social acceptance and improve their quality of life. Hence, people must get access to affordable and high-quality prosthetic technology that gives them functional

and economic independence and allows them to contribute to the country's goal of becoming a developed nation.

The conventional method of prostheses manufacturing involves a tedious measurement process and consultations (Fig. 1). It involves taking manual measurements of the residual limb and then making a positive mould of Gypsum plaster. This mould is further rectified by an expert technician and is finally wrapped with High Density Polyethylene (HDPE) at elevated temperature to make a prosthetic limb of HDPE [5]. The gypsum plaster moulds are of single-use only and generate considerable waste (Fig. 2).



Fig. 1. Tedious Measurement Process



Fig. 2. Single use gypsum plaster moulds

\*Corresponding author: [grsatsangee@gmail.com](mailto:grsatsangee@gmail.com)  
ISSN 0972-5032; Copyright ©2023, SSI

Most users of conventional trans-tibial (below-knee) prosthetic sockets have reported issues with the fit of the prosthetic socket. Some other major problems faced by amputees are skin irritation, abrasion of the stump along the socket (Fig. 3) and regional stress concentration [6].



Fig. 3. Skin irritation due to rough inner surface of the prosthesis

The above-mentioned socio-economic issues and problems faced by the amputees underscore the need for better methods of developing the prosthetic devices. Here, digital manufacturing can be a viable solution. Digital manufacturing integrates 3D scanning, computer-aided-designing (CAD) and additive manufacturing systems to produce cost-effective prostheses with precision. A stepwise process comparison of conventional method and digital manufacturing for making prosthesis is shown in Fig. 4. 3D scanning plays a pivotal role in reverse engineering the lost limbs to speed up prosthesis development and manufacturing. In the conventional method, the amputated region of the patient is covered in plaster to create a measurement cast, and they must wait for the cast to harden. After the cast is hardened, it is removed to the patient, and the gypsum plaster mould is created based on the obtained measurements. This process is manual, and the accuracy of the procedure depends upon the technician's expertise. 3D scanning technology speeds up the process of taking the measurements for the prosthesis and makes the process more efficient and precise.

Additive Manufacturing (AM), commonly known as 3D printing, has been around for nearly three decades and is recognised as a technology that has enormous potential in various fields like manufacturing, biomedical, aerospace, automobile, etc. Many significant advances in this technology have been made with respect to processes, materials and types of printers [7]. Manufacturing prostheses requires complex customizations as each patient's amputations are unique. Additive manufacturing helps enable and accommodate these customisations in a time-saving and cost-effective manner.

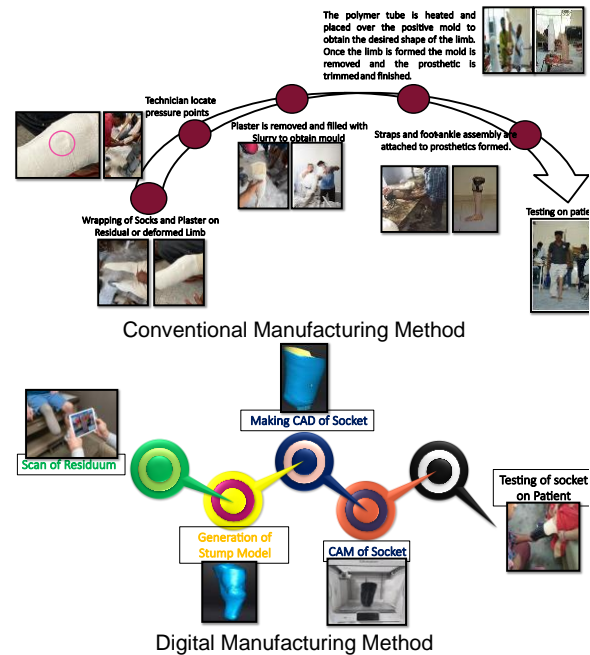


Fig. 4. Comparison of conventional practice and digital manufacturing for prosthesis manufacturing

## II. DIGITAL MANUFACTURING OF THE PROSTHETIC SOCKET

### A. Obtaining 3D scan of the residual limb

A 3D scanner is used to capture the size, shape, and contour of the residual limb (stump) as a high-resolution three-dimensional model (Fig. 5). The stump dimensions were scanned using a textured-light hand-held portable 3D scanner. The scan is further rectified to remove any irregularities in the obtained mesh, such as solid or hollow fill, digital clean-up of extra areas, etc. After rectification, the file is exported to a CAD software such as AutoCAD Fusion 360 or Autodesk Meshmixer for designing the socket.



Fig. 5. 3D Scanning of the residual limb of the amputees

**B. Computer-aided-designing of prosthetic-socket**

The CAD software is used to create a socket that fits the 3D scan of the residual limb and performs rectification on the 3D model of the stump. The socket is sculpted to fit the scan of the stump, with an offset of 2.5 mm, 6 mm thickness and 95% smoothness (Fig. 6 and 7).

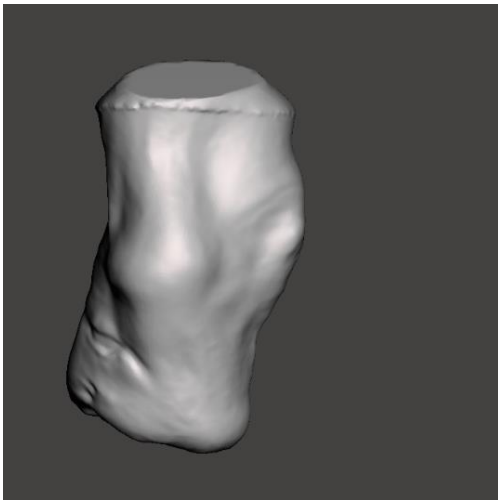


Fig. 6. 3D Scan of the stump in CAD software

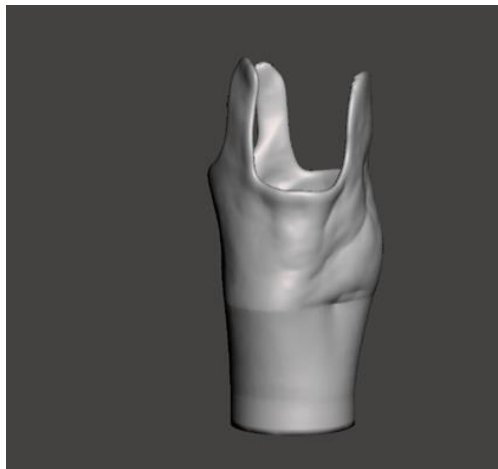


Fig. 7. Socket design in CAD Software

**C. Preparation of digital design for 3D printing**

After the 3D CAD model is finalised, it is exported in STL format, which is the most widely accepted file format for 3D printing systems. The STL file is then sliced layer-by-layer in slicer software such as Simplify3D or Ultimaker Cura (Fig. 8). Required parameters such as printing speed, nozzle temperature, infill density, infill pattern are also decided at this step (Table I).

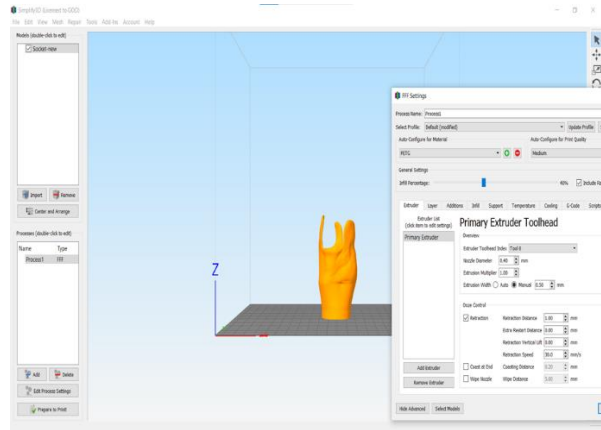


Fig. 8. Slicing of 3D CAD model in simplify 3D slicer software

TABLE I  
3D PRINTING PARAMETERS FOR FABRICATING THE PROSTHESIS

Printing Parameter	Value
Heat bed temperature	65°C
Nozzle Temperature	235°C
Infill density	40%
Infill pattern	Rectilinear
Nozzle Diameter	0.4mm
Printing Speed	45mm/s
Layer Height	0.3mm

**D. 3D Printing of the prosthetic socket**

The slicing software generates the G-codes for the 3D printing machine after finalising the design and printing parameters. These G-codes are sent to the 3D printer for fabrication of the socket. For printing the prosthetic socket, a Fused Filament Fabrication (FFF) printer was used, which is the most widely used and most affordable 3D printer. In an FFF printer, a polymer-based filament is fed through a heated nozzle, which melts the material and deposits it layer-by-layer on the build platform (Fig. 9).

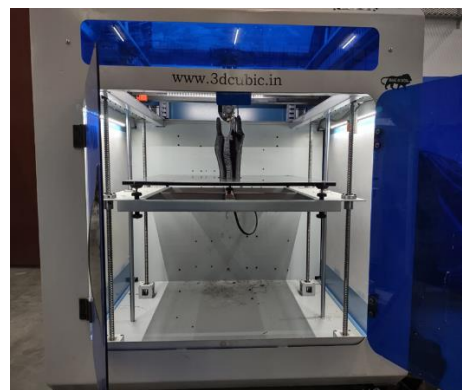


Fig. 9. 3D printing of the prosthetic socket

**E. Post-processing, testing and fine tuning**

Post-processing includes inspection of the printed part, removal of any excess material and smoothening of rough edges and surfaces, if any. Finally, the socket is tested on the amputee and fitting adjustments can be made according to their comfort.

**III. SELECTION OF MATERIAL FOR THE PROSTHETIC SOCKET**

The selection of the material is a crucial factor in the design and manufacturing of the prosthetic socket. It is necessary to select a lightweight material that has strength and durability to withstand the weight of the amputee. Several materials, including Polylactic acid (PLA), Acrylonitrile butadiene styrene (ABS), carbon fibre and metals are being used in the manufacturing of prostheses through additive manufacturing [8-10]. Polyethylene terephthalate glycol (PETG), which is a polymer-based 3D printing filament, is chosen for manufacturing the prostheses due to its superior strength and durability shown over the other polymer-based filaments such as PLA and ABS. PETG is sufficiently flexible to avoid breaking in the layer direction. Excellent layer adhesion while printing results in better surface finishes. Also, PETG is an ideal material for printing large items due to its low shrinking properties [11], [12].

**A. Tensile testing of PETG specimens**

Tensile testing of PETG samples was performed to validate the suitability and mechanical properties of the material. For testing, PETG filament with a diameter of 1.75 mm was used to prepare a standard ASTM D638 Type-IV specimen (Fig. 10). Total 15 samples were prepared for testing with different parameters which can affect the material's mechanical properties, viz. printing nozzle diameter, annealing temperature and time. Six of annealed at 100 °C. The remaining three specimens were not annealed to determine the difference in the properties before and after the annealing process. Details of the specimens are given in Table II.

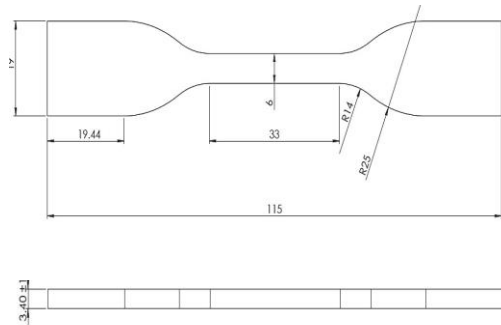


**Fig. 10. ASTM D638 Type-IV Specimen Drawing**

Tensile testing entails applying a pulling force in an

outward direction at both ends of a material and measuring the response. Tensile tests determine how strong a material is and how much it can elongate without permanent distortion (yield) and fracture when subjected to continuous tensile force. Tensile tests are commonly carried out on Universal Testing Machine (UTM) equipment and are thoroughly standardised. The tensile test was performed on a 100 KN UTM machine at the rate of 5 mm/min and the observations obtained are shown in Fig. 12.



**Fig. 11. Specimen after tensile test**

**TABLE II  
SPECIMEN CODE AND PARAMETERS**

Sample No.	Specimen Code	Nozzle Dia. (mm)	Annealing Temp. (°C)	Annealing Time (Min)
1	P1	0.4	NA	NA
2	P2		80	60
3	P3		80	120
4	P4		100	60
5	P5		100	120
6	P6	0.6	NA	NA
7	P7		80	60
8	P8		80	120
9	P9		100	60
10	P10	100	120	
11	P11	0.8	NA	NA
12	P12		80	60
13	P13		80	120
14	P14		100	60
15	P15		100	120

Note: ■ = Samples taken for SEM analysis

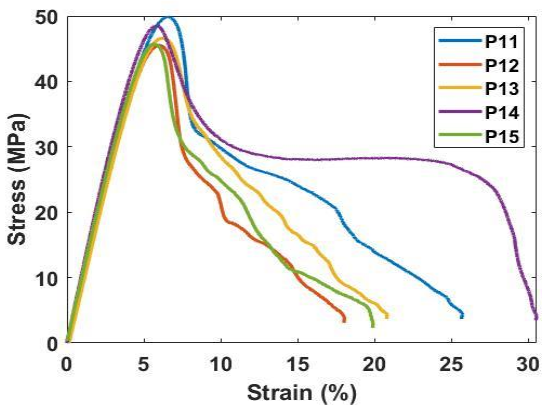
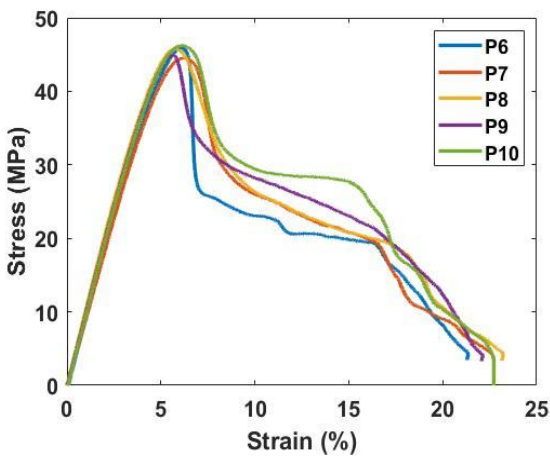
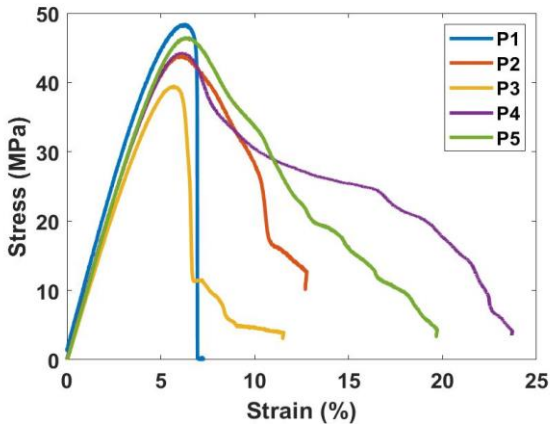


Fig. 12. Stress strains graphs of PETG for different process parameter competition.

**B. SEM analysis of PETG specimens**

A Scanning Electron Microscope (SEM) is a powerful investigative tool that uses a focused electron beam to produce detailed, high magnification images of a sample's surface topography. The high magnification, high-resolution imaging of SEM analysis enables detection of the quantity, size, and form of microscopic particles, which helps to better understand the material's wear

properties. Visual inspection of a surface through SEM can help discover the reasons for failure, material interactions and particle characterization, such as wear debris formed during mechanical wear testing. Fig. 13 shows the SEM fractographic images of the samples 2,3,10,11 & 14 after the tensile testing.

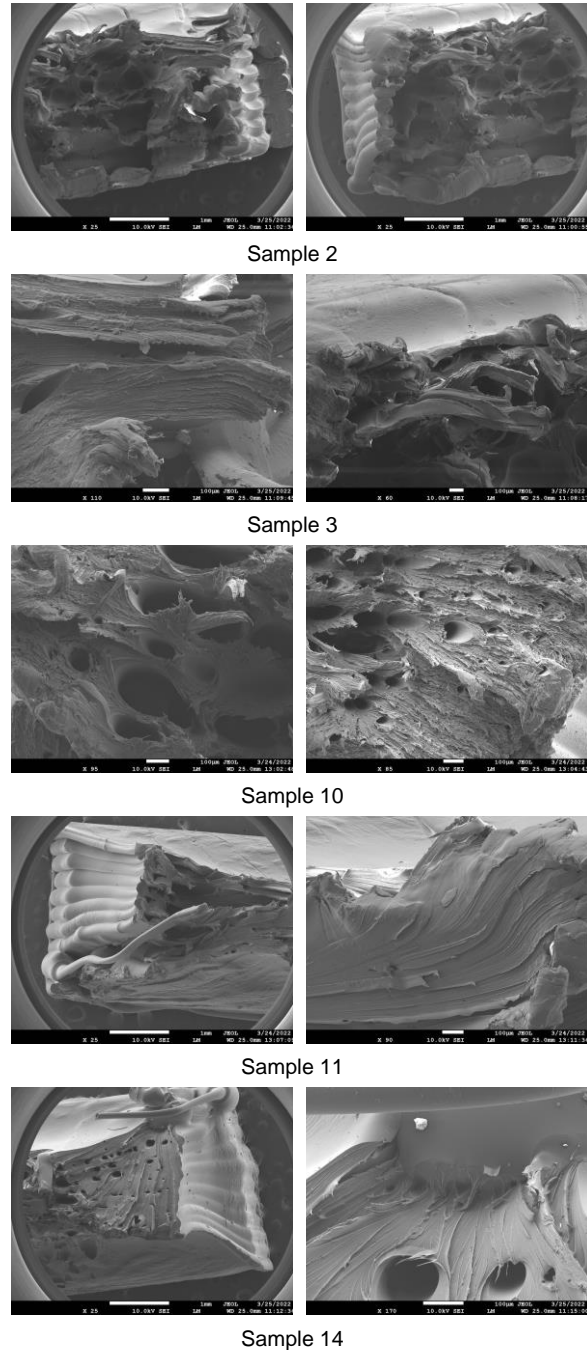


Fig. 13 SEM analysis fractographic images

**C. Results and discussion**

Results of tensile test are summarized in Table III. Peak stresses of PETG samples (in MPa) are shown in Fig. 14.

**TABLE III  
TENSILE TEST RESULTS**

Specimen Code	Peak Stress (MPa)	Peak Load (KN)	Yield Strain (%)	Yield Load (KN)	Elongation at Break Using Strain (%)
P1	48.395	0.871	3.663	0.641	7.232
P2	43.846	0.789	3.753	0.593	12.734
P3	39.479	0.711	3.722	0.547	11.523
P4	44.332	0.798	3.677	0.585	23.714
P5	46.467	0.836	3.91	0.622	19.699
P6	45.99	0.828	3.784	0.603	21.348
P7	44.627	0.803	4.153	0.645	22.728
P8	45.919	0.827	3.625	0.622	23.199
P9	44.942	0.809	3.773	0.63	22.118
P10	46.363	0.835	3.79	0.633	22.669
P11	49.943	0.899	3.778	0.637	25.71
P12	45.626	0.821	4.316	0.696	18.042
P13	46.727	0.841	4.029	0.653	20.811
P14	48.571	0.874	3.613	0.658	30.524
P15	45.796	0.824	3.703	0.64	19.908

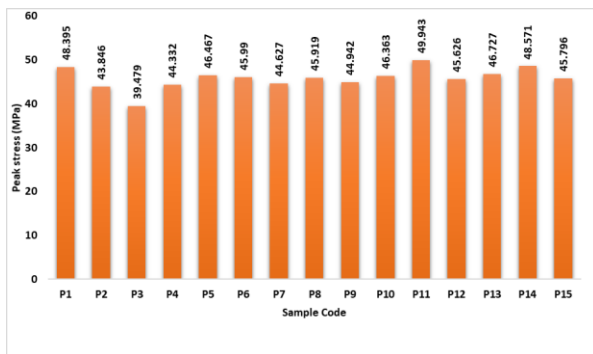


Fig. 14. Peak stresses of PETG samples

As seen in Fig. 12, non-annealed specimen P1 gives the maximum ultimate strength but P4 is more flexible. In general, annealing improves the strength, and the same results can be seen for P10, which gives the highest strength in the same combination of 46.46 MPa. Highest ductility can be seen for the sample P15. As evident from the Table III and Fig. 14, the sample P11 gives the maximum peak strength, which is the PETG sample without annealing and printed with the nozzle of 0.8 mm diameter. There are other samples which give acceptable strength, but they have more chances of pores and

defects. Sample P1 with 0.4 mm diameter and without annealing has second highest peak stress of approximately 48 MPa. Fig. 13 shows the SEM fractographic images of the samples 2,3,10,11 & 14 after the tensile testing. Sample 2 shows some necking points, and a brittle fracture can be seen on the edge of the surface. Some elongation of the material can also be seen. Sample 3 shows detail about layer height and has more layer visibility with small size voids. Largest diameter voids can be seen in sample 10. Sample 11 shows less voids in its fractured surface and its layers are closely packed without any delamination. Layer compression and plastic deformation can be seen in sample 14 with fibre pulls and large voids. Considering the results of tensile test and SEM analysis, PETG sample without annealing and with 0.4 mm printing nozzle diameter is chosen for making the prosthetic socket.

**IV. ADVANTAGES OF DIGITAL MANUFACTURING OVER THE CONVENTIONAL METHOD FOR MAKING PROSTHESIS**

**A. Comfort and ease of use**

Because of socket discomfort, traditional prosthetic limbs are known to be cumbersome. AM-produced prosthetics are more user-customisable and far lighter and more comfortable.

**B. Time, speed and agility**

While traditional prosthetics can take weeks or even months to produce and calibrate, AM prosthetics can be created in as little as one day, making the process more efficient.

**C. Customisation**

AM allows users to create specific shapes and sizes, resulting in a highly customisable prosthetic. AM also enables more versatile prosthetics for a variety of purposes and activities.

**D. Accessibility**

The advent of the additive manufacturing process makes it easier to create various types of prosthetics that could reach a much larger population than before.

**E. Cost of the prosthetics**

Commercially produced prosthetics are currently expensive. Many physically unique people require prosthetics but lack the financial means to do so, forcing them to lead a limited life. On the other hand, AM-produced prosthetics are inexpensive to produce and affordable. These prosthetics typically cost much less than high-end prosthetic devices available in the market and would be viable for people looking to improve their lives significantly.

## V. CONCLUSION AND FUTURE AREAS OF RESEARCH

Digital manufacturing tools like additive manufacturing and 3D scanning open numerous opportunities for fabricating customised prostheses. This study proposes the process and design for an affordable customised prosthetic socket, and it is manufactured using state-of-the-art digital manufacturing tools. Accessibility to customised prostheses at a reasonable cost will enable the financially weak amputees of the country to regain confidence and lead a normal life. Despite the advantages, some limitations regarding the useability of prosthetic sockets fabricated through additive manufacturing may still be identified. Material selection is an essential factor for fabricating a functional prosthesis. In the case of children, traditional prosthetics become obsolete and must be replaced as they grow, and their bodies change. Replacing the prosthetic limb to keep up with the growth rate until the physically unique individual reaches maturity can be costly. Researchers are currently working on prosthetics made of expandable and functional materials that will evolve as the user's body changes. In future, follow-up studies must be conducted with the amputees using a digitally manufactured prosthesis to understand these and other limitations in depth and overcome them.

## ACKNOWLEDGMENTS

Support from TEQIP -III, Faculty of Engineering, DEI is highly appreciated. The authors acknowledge the grant received from AICTE (file no. 8-88/FDC/RPS (POLICY-1)/2019-20). Support of Hardayal Viklang Sahayta Kendra, Agra is also acknowledged.

## REFERENCES

- [1] Dadkhah, B., Valizadeh, S., Mohammadi, E., & Hassankhani, H. (2013). Psychosocial adjustment to lower-limb amputation: A review article. *HealthMED*, 7(2), 502-507.  
<https://doi.org/10.1080/09638280410001708869>
- [2] Mohan D. (1986). A Report on Amputees in India. *Orthotics and Prosthetics* 40, 16-32.  
[http://www.oandplibrary.org/op/1986\\_01\\_016.asp](http://www.oandplibrary.org/op/1986_01_016.asp)
- [3] Census (2011). Primary Census Abstracts, Registrar General of India, Ministry of Home Affairs, Government of India <https://censusindia.gov.in/census.website/>
- [4] Sahu, A., Sagar, R., Sarkar, S., & Sagar, S. (2016). Psychological effects of amputation: A review of studies from India. *Industrial psychiatry journal*, 25(1), 4-10.  
<https://doi.org/10.4103/0972-6748.196041>
- [5] Bhargava R. (2019). The Jaipur Foot and the "Jaipur Prosthesis". *Indian journal of orthopaedics*, 53(1), 5-7.  
[https://doi.org/10.4103/ortho.IJOrtho\\_162\\_18](https://doi.org/10.4103/ortho.IJOrtho_162_18)
- [6] Chatterjee et al. (2016). Review: Problems with Use of Trans-Tibial Prosthesis. *Journal of Medical Imaging and Health Informatics*. 6. 269-284.  
<https://doi.org/10.1166/jmihi.2016.1686>.
- [7] Pérez, M., Carou, D., Rubio, E. M., & Teti, R. (2020). Current advances in additive manufacturing. *Procedia Cirp*, 88, 439-444.  
<https://doi.org/10.1016/j.procir.2020.05.076>
- [8] Sam, M. et al. (2004). The 'shape&roll' prosthetic foot: I. Design and development of appropriate technology for low-income countries. *Medicine, conflict, and survival*, 20(4), 294-306.  
<https://doi.org/10.1080/1362369042000285937>
- [9] Martulli et al. (2023). Preliminary Stiffness-Driven Redesign of a Laminated Prosthetic Component Using Additive Manufacturing. *Polymers*. 15.  
<https://doi.org/10.3390/polym15020346>
- [10] Rochlitz, B., & Pammer, D. (2017). Design and analysis of 3D printable foot prosthesis. *Periodica Polytechnica Mechanical Engineering*, 61(4), 282-287.  
<https://doi.org/10.3311/PPme.11085>
- [11] Szykiedans, K., Credo, W., & Osiński, D. (2017). Selected mechanical properties of PETG 3-D prints. *Procedia Engineering*, 177, 455-461.  
<https://doi.org/10.1016/j.proeng.2017.02.245>
- [12] Waly, C., Petersmann, S., & Arbeiter, F. (2023). Multimaterial Extrusion-Based Additive Manufacturing of Compliant Crack Arrestor: Influence of Interlayer Length, Thickness, and Applied Strain Rate. *Advanced Engineering Materials*, 25(7), 2101703.  
<https://doi.org/10.1002/adem.202101703>

# Femtosecond Photonic Logic Gates with MoTe<sub>2</sub> Nanocomposite Thin Films

Anam Saifi and Sukhdev Roy\*

Department of Physics and Computer Science,  
Dayalbagh Educational Institute, Agra-282005, Uttar Pradesh, India

*A detailed theoretical analysis of ultrafast saturable absorption (SA) and reverse saturable absorption (RSA) has been presented in MoTe<sub>2</sub> thin films with femtosecond (fs) laser pulses at 800 nm. With an increase in pulse intensity, the switching contrast increases due to high nonlinear absorption. Theoretical results are in good agreement with reported experimental results. The effect of pump pulse intensity, pulse width, NLA coefficient and sample thickness has been studied to optimize the SA and RSA transition. Also, the results for low-power and high contrast all-optical switching in MoTe<sub>2</sub> nanofilms have been used to design all-optical fs universal NOR and NAND logic gates. The study demonstrates the applicability of transition metal dichalcogenides for ultrafast all-optical information processing.*

**Keywords** – Nonlinear absorption, Transition metal dichalcogenides, All-optical switching, Ultrafast dynamics, All-optical logic gates, Ultrafast information processing

## I. INTRODUCTION

The requirement for ultrafast and ultrahigh bandwidth information processing has provided tremendous impetus to design, synthesize and characterize the nonlinear optical (NLO) response of different molecular configurations. The wide range of materials studied for various photonic applications include, chromophores, phthalocyanines, porphyrins, rhodopsins, dyes, semi-conductor-doped glasses, fullerenes, graphene, graphene based composites, MXenes and transition metal dichalcogenides [1]–[11]. The basic challenge is to design an energy-efficient all-optical switch that exhibits ultra-fast response time, high contrast, low-power operation, high photo and thermal stability in a broad spectral range, is ultra-compact, cost-effective, has logic-level restoration, good noise margin, better fan-out, scalability, cascability and compatibility with other materials along with the flexibility to tailor the photoresponse to meet device specifications [12]. There is tremendous research effort focused on designing all-optical computing units for next-generation high speed and high bandwidth photonic computation [13].

Recently, transition metal dichalcogenides (TMDCs) have emerged as excellent materials that have tunable bandgaps that change from indirect to direct bandgap semiconductors. TMDCs are atomically thin semi-conductors of the form MX<sub>2</sub>, where M is the transition metal atom from groups IV-X of the periodic table and X is a chalcogen atom from group 16 of the periodic classification [14]. Monolayer TMDCs consist of a single layer of transition metal atoms sandwiched between two layers of chalcogen atoms to form X-M-X type structure held together by Van-der-Waals forces combined with a covalent bond [15].

Semiconductor TMDCs have bandgaps in the near-infrared to the visible region [16] and offer electrical, optical, mechanical properties, chemical stability, large thermal threshold, cost-effectiveness and nonlinear processes such as harmonic generation, four-wave mixing, saturable absorption (SA), reverse saturable absorption (RSA) and two-photon absorption [17]. The wide range of applications include high-end electronics, spintronics, photovoltaics, energy harvesting, ultra-sensitive photodetectors, large scale solar cell applications, light-emitting devices, flexible devices, DNA sequencing, sensors, biosensors, bio-medical applications and personalized medicines [14], [18], [19].

Heterostructures based on 2D TMDCs are important due to prospective applications as p-n junctions, field-effect transistors (FETs), opto-valleytronic devices and photovoltaic cells [20], [21]. Although, all 2D TMDCs exhibit potential for optoelectronics applications, their heterostructures show remarkable properties that may not occur in their constituent layers [22]. The formation of vdW heterostructures by TMDCs and other materials provides good photo response and opens up prospects for developing novel devices with desired optoelectronic properties [21–23].

Logic gates are the basic building block of computing circuits. For a variety of materials, SA characteristics have been used to design all-optical AND, OR logic gates whereas RSA characteristics have been used for the NOT gate and universal NAND, NOR logic gates by considering appropriate threshold. Interestingly, it has been shown that SA to RSA transition occurs in thick films on changing the thickness of the sample using fs laser pulses at 800 nm [24], which is advantageous in the simultaneous realization of various all-optical logic gates.

Hence, the objective of this paper is, (1) to study the ultrafast nonlinear absorption in MoTe<sub>2</sub> nanocomposite thin

\*Corresponding author: [sukhdevroy@dei.ac.in](mailto:sukhdevroy@dei.ac.in)  
ISSN 0972-5032 (P), Copyright ©2023, SSI

films, (2) to determine optimized conditions with respect to pulse width, absorption cross-section, excitation intensity and sample thickness (3) to design all-optical ultrafast logic gates and (4) compare the all-optical switching behavior.

## II. THEORETICAL MODEL

### A. Theoretical Model for MoTe<sub>2</sub>

Ultrafast nonlinear absorption (NLA) in MoTe<sub>2</sub> thin films can be described by the four-level energy diagram as shown in Fig.(1) [24]. The excitation and de-excitation processes lead to the following rate equations for different energy states:

$$\frac{dN_0}{dt} = -\frac{\sigma_0 N_0 I}{h\nu} + \frac{N_1}{\tau_1} \quad (1)$$

$$\frac{dN_1}{dt} = \frac{\sigma_0 N_0 I}{h\nu} - \frac{N_1}{\tau_1} - \frac{\sigma_1 N_1 I}{h\nu} + \frac{N_2}{\tau_2} \quad (2)$$

$$\frac{dN_2}{dt} = \frac{\sigma_1 N_1 I}{h\nu} - \frac{N_2}{\tau_2} - \frac{\sigma_2 N_2 I}{h\nu} + \frac{N_3}{\tau_3} \quad (3)$$

$$\frac{dN_3}{dt} = \frac{\sigma_2 N_2 I}{h\nu} - \frac{N_3}{\tau_3} \quad (4)$$

where  $N_0, N_1, N_2$  and  $N_3$  represent population densities of energy states  $S_0, S_1, S_2$  and  $S_3$  respectively.  $\sigma_0, \sigma_1$  and  $\sigma_2$  are the absorption cross-sections of  $S_0 \rightarrow S_1, S_1 \rightarrow S_2$  and  $S_2 \rightarrow S_3$  respectively, and  $\tau_1, \tau_2$  and  $\tau_3$  are excited state lifetimes as shown in Fig. 1.

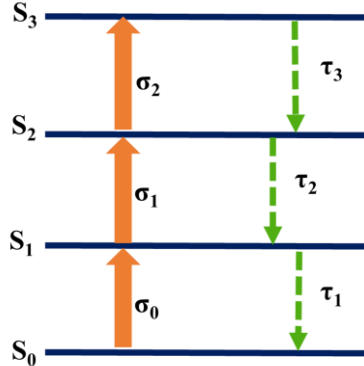


Fig. 1. Four level energy diagram for MoTe<sub>2</sub> [24]

The transmitted intensity through the MoTe<sub>2</sub> sample is given by,

$$\frac{dI}{dz} = -\alpha(I)I \quad (5)$$

where  $\alpha(I) = \alpha_0 + \alpha_{NL}I$ ,  $\alpha_0$  is the linear absorption coefficient and  $\alpha_{NL}$  is the nonlinear absorption coefficient.

A Gaussian modulating laser pulse is considered to excite the sample which is given by,

$$I = I_0 \left( \frac{\omega_0^2}{\omega^2(z)} \right) \exp\left(-\frac{t^2}{\tau_p^2}\right) \exp\left(-\frac{2r^2}{\omega^2(z)}\right) \quad (6)$$

$$\text{where } \omega(z) = \omega_0 \left( 1 + \left( \frac{z}{z_0} \right)^2 \right)^{1/2}$$

$z_0 = \frac{\pi\omega_0^2}{\lambda}$ ,  $\omega_0$  is the radius of beam waist,  $\tau_p$  is the input pulse width and  $I_0$  is the peak input intensity.

## III. RESULTS AND DISCUSSION

NLA has been studied through numerical simulations using equations (1-6) for MoTe<sub>2</sub> thin films by considering reported experimental parameters [24]. We consider a laser pulse from Ti : Sapphire femtosecond laser at 800 nm to excite the sample with beam waist 30  $\mu\text{m}$ . The absorption cross-sections and lifetimes experimentally reported for ps regime are  $\sigma_0 = 9.5 \times 10^{-15} \text{ cm}^2$ ,  $\sigma_1 = 0.15 \sigma_0$ ,  $\sigma_2 = 0.16 \sigma_1$ ,  $\tau_1 = 16.76 \text{ ps}$ ,  $\tau_2 = 0.002 \text{ ps}$ ,  $\tau_3 = 0.016 \text{ ps}$  and sample thickness 80 nm [24].

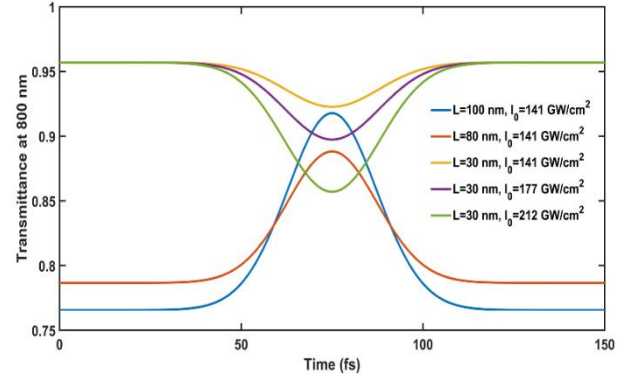


Fig. 2. Theoretical simulation of the transmittance of MoTe<sub>2</sub> with time at wavelength 800 nm and pulse width 35 fs.

The effect of intensity on transmittance at different peak pump intensities is shown in Fig. 2, Fig. 3 and Fig. 4. It is evident that the transmittance and percentage modulation increase with increase in  $I_0$ , as more molecules get excited from the ground state to the higher excited-states.

NLO response is also sensitive to the sample thickness. Interestingly, it can be seen from the Fig. 5 and Fig. 6 that at different values of sample thickness, keeping input intensity fixed at  $I_0 = 500 \text{ GW/cm}^2$ , the switching contrast increases with increase in sample thickness. This could be due to the coupling of layers in the films which could influence exciton formation, relaxation and transport of charge carriers [25]–[27].

Two-input all-optical OR and AND logic gates have been theoretically designed by optimising the contrast to be as high possible with sample thickness and intensity using fs pulses at 800 nm and  $I_0 = 303 \text{ GW/cm}^2$  with pure MoTe<sub>2</sub>, MoS<sub>2</sub> films and MoTe<sub>2</sub>/MoS<sub>2</sub> nanocomposite films as shown in Fig. 7.

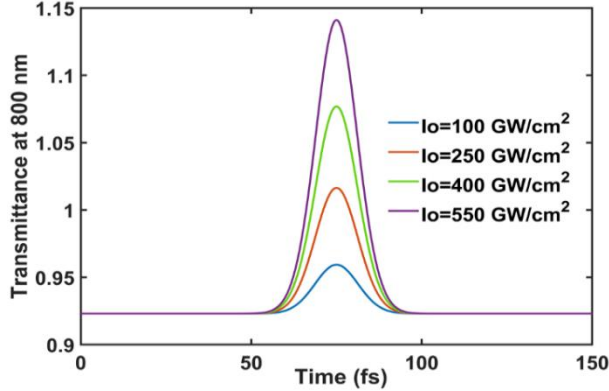


Fig. 3. Variation of transmittance with time for MoTe<sub>2</sub> for a pulse at 800 nm, pulse width 15 fs for different pulse intensities for SA behaviour, sample thickness = 100 nm,  $\alpha_0 = 2.67 \times 10^4 \text{ cm}^{-1}$ ,  $\alpha_{NL} = -128.51 \text{ cm/GW}$

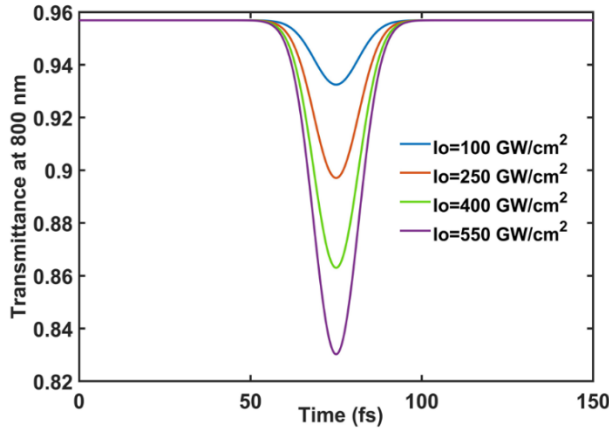


Fig. 4. Variation of transmittance with time for MoTe<sub>2</sub> for a pulse at 800 nm, pulse width 15 fs for different pulse intensities for RSA behaviour, sample thickness = 30 nm,  $\alpha_0 = 1.47 \times 10^4 \text{ cm}^{-1}$ ,  $\alpha_{NL} = 86.04 \text{ cm/GW}$

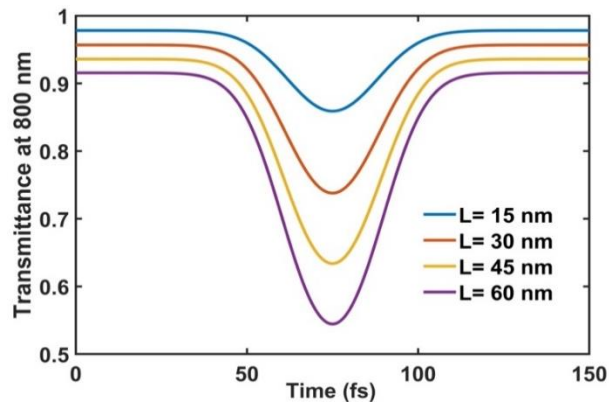


Fig. 5. Variation of transmittance with time for MoTe<sub>2</sub> during a single laser pulse of wavelength 800 nm, pulse width 35 fs for different sample thickness for RSA behaviour at  $I_0 = 500 \text{ GW/cm}^2$ ,  $\alpha_0 = 1.47 \times 10^4 \text{ cm}^{-1}$ ,  $\alpha_{NL} = 86.04 \text{ cm/GW}$ .

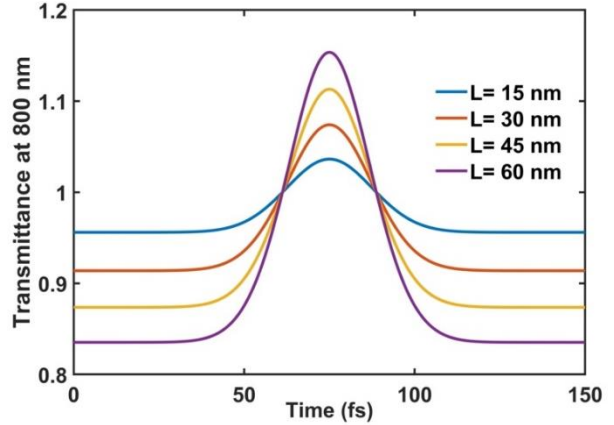


Fig. 6. Variation of transmittance with time for MoTe<sub>2</sub> during a single laser pulse of wavelength 800 nm, pulse width 35 fs for different sample thickness for SA behaviour at  $I_0 = 500 \text{ GW/cm}^2$ ,  $\alpha_0 = 3 \times 10^4 \text{ cm}^{-1}$ ,  $\alpha_{NL} = -107.63 \text{ cm/GW}$ .

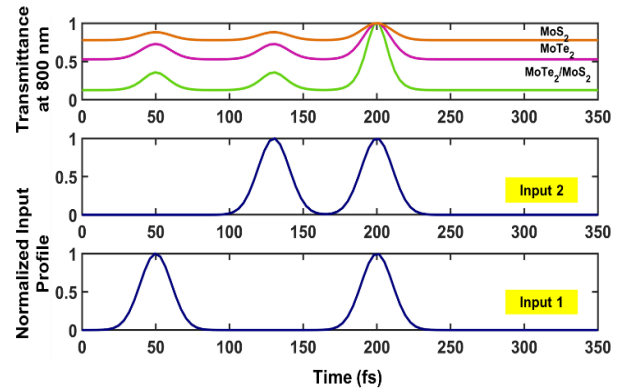
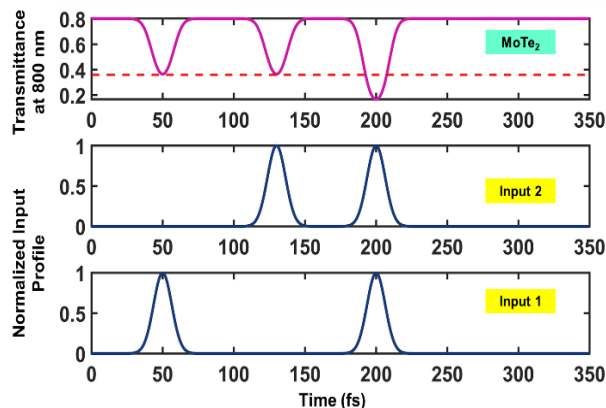


Fig. 7. Design of All-Optical OR (without threshold) and AND (with threshold) Logic Gates with  $I_0 = 303 \text{ GW/cm}^2$ , Wavelength = 800 nm and  $\tau_p = 15 \text{ fs}$

For two-input all-optical OR logic realization, when no input is present, the output is zero or low and when either one or both inputs are present the output is high. The threshold value for MoS<sub>2</sub> and MoTe<sub>2</sub> nanocomposite films is 0.88 and 0.72 respectively. Similarly, for two-input all-optical NOR logic realization, when no input is present the output is high and when either one or both inputs are present the output is low. NOR and NAND logic have been realised by optimising RSA of MoTe<sub>2</sub> films by considering the threshold at 0.36 (dashed line). NAND logic can be realised as and when both the inputs are high simultaneously, output transmittance is low and above threshold it is considered to be high.

#### IV. CONCLUSION

A detailed theoretical analysis of ultrafast nonlinear absorption such as RSA and SA with TMDCs has been carried out. The characteristics are sensitive to peak intensity, sample thickness, wavelength, pulse-width and absorption cross-section.



**Fig. 8. Design of All-Optical Logic Gates (dashed line as threshold at 0.36) for MoTe<sub>2</sub> thin films: NAND (without threshold) and NOR (with threshold) with  $I_0 = 303 \text{ GW/cm}^2$ , Sample thickness = 150 nm and  $\tau_P = 15 \text{ fs}$**

The SA and RSA behaviour of TMDCs films has been utilized to design ultrafast all-optical logic gates. The NLO properties of TMDCs can be tailored by various techniques that include, varying sample thickness and chemical composition or covalently functionalizing it with materials that exhibit large optical nonlinearities. The proposed all-optical logic gates can be realized by only controlling pulse intensity with the same sample thickness and wavelength, instead of using a pump-probe configuration. They are also advantageous due to simplicity, tunability, controllability, photo-thermal stability, scalability and digital simple operation. The study opens up prospects for transition metal dichalcogenides for ultrafast NLA and all-optical switching-based applications.

### ACKNOWLEDGMENTS

The authors express their gratitude to Professor P.S. Satsangi for his kind inspiration and encouragement. They acknowledge the University Grants Commission, India, for the Special Assistance Programme Grant No. [F.530/14/DRS-III/2015(SAP-I)]. Anam Saifi and Professor Sukhdev Roy thank Department of Science and Technology, India, for the award of the INSPIRE Fellowship (DST/INSPIRE/03/2021/001130) and research projects CRG/2021/005139 and MTR/2021/000742, respectively.

### REFERENCES

- [1] Arshad, M. N. et al. (2022). Donor moieties with D- $\pi$ -a framing modulated electronic and nonlinear optical properties for non-fullerene-based chromophores. *RSC advances*, 12(7), 4209-4223.
- [2] Fathima, R., & Mujeeb, A. (2021). Plasmon enhanced linear and nonlinear optical properties of natural curcumin dye with silver nanoparticles. *Dyes and Pigments*, 189, 109256.
- [3] Jeyaram, S., & Geethakrishnan, T. (2020). Spectral and third-order nonlinear optical characteristics of natural pigment extracted from coriandrum sativum. *Optical Materials*, 107, 110148.
- [4] Roy, S., & Yadav, C. (2011). All-optical ultrafast logic gates based on saturable to reverse saturable absorption

- transition in CuPc-doped PMMA thin films. *Optics Communications*, 284(19), 4435-4440.
- [5] Roy, S., & Yadav, C. (2014). All-optical sub-ps switching and parallel logic gates with bacteriorhodopsin (BR) protein and BR-gold nanoparticles. *Laser Physics Letters*, 11(12), 125901.
- [6] Sharma, P., Roy, S., & Singh, C. P. (2005). Dynamics of all-optical switching in polymethine dye molecules. *Thin Solid Films*, 477(1-2), 42-47.
- [7] Sharma, P., & Roy, S. (2004). All-optical light modulation in pharaonis phoborhodopsin and its application to parallel logic gates. *Journal of applied physics*, 96(3), 1687-1695.
- [8] Yadav, C., & Roy, S. (2015). Ultrafast all-optical universal logic gates with graphene and graphene-oxide metal porphyrin composites. *Journal of Computational Electronics*, 14, 209-213.
- [9] Yadav, C., & Roy, S. (2016). Ultrafast nonlinear absorption in hemoprotein cytochrome-c and its application to computing. *Optical and Quantum Electronics*, 48, 1-11.
- [10] Yadav, C., & Roy, S. (2017). Optimization of ultrafast reverse saturable to saturable absorption transition in Ru dioxolene complex for all-optical logic applications. *Optical and Quantum Electronics*, 49, 1-11.
- [11] Yahya, M., Nural, Y., & Seferoğlu, Z. (2022). Recent advances in the nonlinear optical (NLO) properties of phthalocyanines: A review. *Dyes and Pigments*, 198, 109960.
- [12] Feng, L., Wang, Z., Wang, W., Li, F., Ren, Y., & Wang, Y. (2022). Constructing Urbach-Tail-Free and Low-Threshold Perovskite Heteronanowire Lasers toward All-Optical Switching. *ACS Photonics*, 9(2), 459-465.
- [13] Goswami, K., Mondal, H., & Sen, M. (2021). A review on all-optical logic adder: Heading towards next-generation processor. *Optics Communications*, 483, 126668.
- [14] Manzeli, S., Ovchinnikov, D., Pasquier, D., Yazyev, O. V., & Kis, A. (2017). 2D transition metal dichalcogenides. *Nature Reviews Materials*, 2(8), 1-15.
- [15] Mattheiss, L. F. (1973). Band structures of transition-metal-dichalcogenide layer compounds. *Physical Review B*, 8(8), 3719.
- [16] Yu, J. et al. (2021). Giant nonlinear optical activity in two-dimensional palladium diselenide. *Nature communications*, 12(1), 1083.
- [17] Wen, X., Gong, Z., & Li, D. (2019). Nonlinear optics of two-dimensional transition metal dichalcogenides. *InfoMat*, 1(3), 317-337.
- [18] Anju, S., & Mohanan, P. V. (2021). Biomedical applications of transition metal dichalcogenides (TMDCs). *Synthetic Metals*, 271, 116610.
- [19] Xu, H., Lin, Z., & Dai, X. (2022). MoTe<sub>2</sub> quantum dots-based all-optical switching. *Optics Communications*, 506, 127573.
- [20] Liao, G. et al. (2023). Synthesis and Application of Liquid Metal Based-2D Nanomaterials: A Perspective View for Sustainable Energy. *Molecules*, 28(2), 524.
- [21] Somvanshi, D., & Jit, S. (2020). Transition metal dichalcogenides based two-dimensional heterostructures for optoelectronic applications. In *2D Nanoscale Heterostructured Materials* (pp. 125-149). Elsevier.
- [22] Li, M. Y., Chen, C. H., Shi, Y., & Li, L. J. (2016). Heterostructures based on two-dimensional layered materials and their potential applications. *Materials Today*, 19(6), 322-335.
- [23] Quan, C. et al. (2019). Band alignment of MoTe<sub>2</sub>/MoS<sub>2</sub> nanocomposite films for enhanced nonlinear optical performance. *Advanced Materials Interfaces*, 6(5), 1801733.
- [24] Quan, C. et al. (2018). Transition from saturable absorption to reverse saturable absorption in MoTe<sub>2</sub> nano-films with thickness and pump intensity. *Applied Surface Science*, 457, 115-120.

- [25] Jiang, Y., Chen, S., Zheng, W., Zheng, B., & Pan, A. (2021). Interlayer exciton formation, relaxation, and transport in TMD van der Waals heterostructures. *Light: Science & Applications*, 10(1), 72.
- [26] Synnatschke, K. et al. (2019). Length-and thickness-dependent optical response of liquid-exfoliated transition metal dichalcogenides. *Chemistry of Materials*, 31(24), 10049-10062.
- [27] Alexeev, E. M. et al. (2017). Imaging of interlayer coupling in van der Waals heterostructures using a bright-field optical microscope. *Nano letters*, 17(9), 5342-5349.

# APPENDIX

## NSC-2022 CONFERENCE COMMITTEE

### CHIEF PATRON

**Prof. P. S. Satsangi**

*Chairman*

Advisory Committee on Education

Dayalbagh Educational Institutions, Dayalbagh, Agra 282005

### PATRON

**Prof. P.K. Kalra**

*Director*

Dayalbagh Educational Institute, Dayalbagh, Agra 282005

### INTERNATIONAL ADVISORY COMMITTEE

Shri. G.S. Sood, President, DEI  
Prof. Peter H. Roe, University of Waterloo, Canada  
Prof. Keith W. Hipel, University of Waterloo, Canada  
Prof. Ajit K. Srivastava, Michigan State University, USA  
Prof. Geoff Simm, University of Edinburgh, UK  
Prof. Digvir S. Jayas, University of Manitoba, Canada  
Prof. Anand Srivastava, Kiel University, Germany  
Prof. Anna M. Horatchek, Kiel University, Germany  
Dr. Manu Prakash, Stanford University, USA  
Prof. Karmeshu, University of Petroleum and Energy Studies, Dehradun  
Prof. Huzur Saran, IIT Delhi  
Shri. M.A. Pathan, Former Chairman Indian Oil Corporation Ltd.  
Prof. Pami Dua, Delhi School of Economics  
Dr. Bhupinder Singh, Indian Agricultural Research Institute, Delhi  
Dr. K. Usha, Indian Agricultural Research Institute, Delhi  
Prof. Prem Kumar Kalra, IIT Delhi, President, SSI  
Prof. C. Patvardhan, DEI, Vice-President, SSI  
Prof. D. Bhagwan Das, DEI, Secretary, SSI

### PROGRAM AND ORGANISING COMMITTEE

Dr. Prem Sevak Sudhish, DEI (Convener)  
Prof. Sanjay Bhushan, DEI  
Smt. Sneha Bijlani, DEI  
Dr. Sanil Kumar, DEI  
Shri. V. Deepak, DEI  
Dr. Amla Chopra, DEI  
Dr. Shiroman Prakash, DEI  
Shri. Gaurav Pratap Rana, DEI  
Dr. Sushma Mishra, DEI  
Dr. Prem Shankar Singh, DEI

Dr. Ankit Sahai, DEI (Convener)  
Dr. Ashok Yadav, DEI  
Dr. Jaspreet Kaur, DEI  
Dr. Dheeraj Kumar Angjala, DEI  
Dr. Sonal Singh, DEI  
Dr. Rajeev Kumar Chauhan, DEI  
Shri. Manish Kumar, DEI  
Dr. Purnima Bhatnagar, DEI  
Dr. Gufran Ahmad, DEI

## SESSION CHAIRS

Dr. Dayal Pyari Srivastava, DEI  
Prof. Sukhdev Roy, DEI  
Dr. N. Apurva Ratan Murty, MIT  
Dr. Aatmesh Srivastava, DEI  
Dr. Bhupinder Singh, IARI  
Dr. Raj Kamal Bhatnagar, ICGEB (Retired)  
Dr. Anjoo Bhatnagar, DEI  
Prof. G.S.S. Babu, DEI  
Prof. Sona Ahuja, DEI

Dr. Bani Dayal Dhir, DEI  
Dr. Nirat Ray, IIT Delhi  
Dr. Sonal Sahai, DEI  
Prof. G.P. Satsangi, DEI  
Dr. Rohit Srivastava, DEI  
Dr. Rajiv Ranjan, DEI  
Prof. Kamal Srivastava, DEI  
Dr. S.K. Soni, DEI  
Prof. Pravin Saxena, DEI